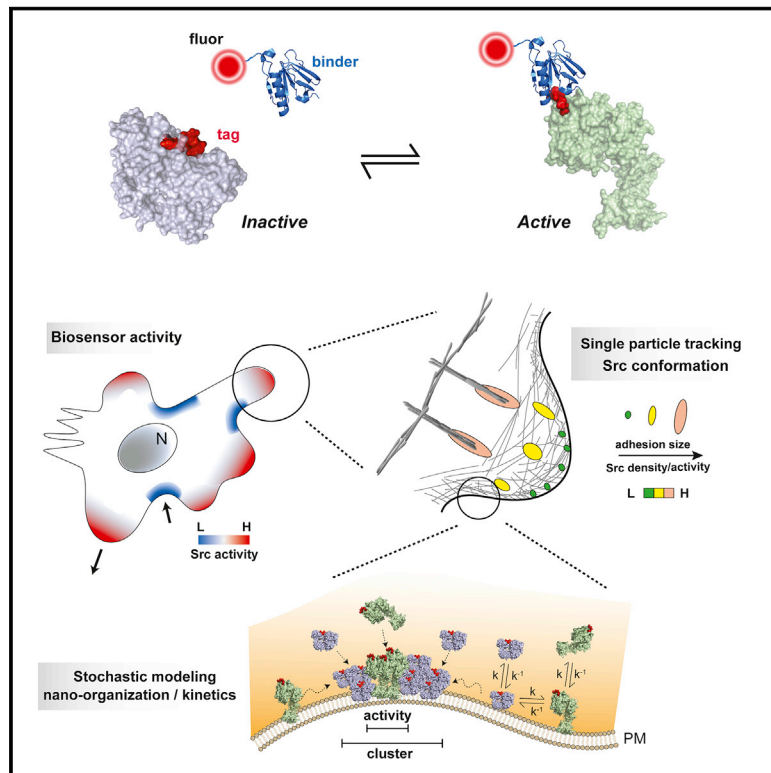


Biosensors based on peptide exposure show single molecule conformations in live cells

Graphical abstract



Authors

Bei Liu, Orrin J. Stone, Michael Pablo, ..., Luke D. Lavis, Timothy C. Elston, Klaus M. Hahn

Correspondence

timothy_elston@med.unc.edu (T.C.E.), khahn@med.unc.edu (K.M.H.)

In brief

Biosensors responding to protein conformation enable single molecule detection of active proteins in live cells, affording insights into both cellular function and organization.

Highlights

- Generalizable biosensors based on changes in exposure of small peptides
- A bright signal enables detection of single molecule conformations in living cells
- Conformation is revealed by FRET or simply by localization of a fluorophore
- Quantitation of Src dynamics and activation in clusters and at adhesions



Resource

Biosensors based on peptide exposure show single molecule conformations in live cells

Bei Liu,^{1,7} Orrin J. Stone,^{1,7} Michael Pablo,^{2,3,7} J. Cody Herron,^{4,6} Ana T. Nogueira,¹ Onur Dagliyan,¹ Jonathan B. Grimm,⁵ Luke D. Lavis,⁵ Timothy C. Elston,^{1,4,6,*} and Klaus M. Hahn^{1,6,8,*}

¹Department of Pharmacology, University of North Carolina at Chapel Hill, Chapel Hill, NC 27599, USA

²Department of Chemistry, University of North Carolina at Chapel Hill, Chapel Hill, NC 27599, USA

³Program in Molecular and Cellular Biophysics, University of North Carolina at Chapel Hill, Chapel Hill, NC 27599, USA

⁴Curriculum in Bioinformatics and Computational Biology, University of North Carolina at Chapel Hill, Chapel Hill, NC 27599, USA

⁵Janelia Research Campus, The Howard Hughes Medical Institute, Ashburn, VA 20147, USA

⁶Computational Medicine Program, University of North Carolina at Chapel Hill, Chapel Hill, NC 27599, USA

⁷These authors contributed equally

⁸Lead contact

*Correspondence: timothy_elston@med.unc.edu (T.C.E.), khahn@med.unc.edu (K.M.H.)

<https://doi.org/10.1016/j.cell.2021.09.026>

SUMMARY

We describe an approach to study the conformation of individual proteins during single particle tracking (SPT) in living cells. “Binder/tag” is based on incorporation of a 7-mer peptide (the tag) into a protein where its solvent exposure is controlled by protein conformation. Only upon exposure can the peptide specifically interact with a reporter protein (the binder). Thus, simple fluorescence localization reflects protein conformation. Through direct excitation of bright dyes, the trajectory and conformation of individual proteins can be followed. Simple protein engineering provides highly specific biosensors suitable for SPT and FRET. We describe tagSrc, tagFyn, tagSyk, tagFAK, and an orthogonal binder/tag pair. SPT showed slowly diffusing islands of activated Src within Src clusters and dynamics of activation in adhesions. Quantitative analysis and stochastic modeling revealed *in vivo* Src kinetics. The simplicity of binder/tag can provide access to diverse proteins.

INTRODUCTION

Fluorescent biosensors have provided a valuable window into the behavior of proteins within living cells, but their limitations have become increasingly apparent. They can be difficult to engineer—Förster resonance energy transfer (FRET) requires introduction of two fluorescent proteins where they respond to conformational change but do not perturb normal activity. When biosensors are based on protein fragments that bind specifically to one structural state, the fragments often compete with endogenous ligands. The indirect excitation of FRET reduces fluorescence intensity, necessitating higher concentrations that can perturb cells and lead to greater phototoxicity/photobleaching. Brighter biosensors could enable visualization of low abundance proteins without perturbation, and visualization of single molecule conformational changes in living cells. FRET is usually too dim for single molecule studies in cells (Jares-Erijman and Jovin, 2003). It has been used successfully by labeling proteins with bright dyes and reintroducing them into cells (König et al., 2015; Sakon and Weninger, 2010), and nucleotide binding to a GTPase was reported by FRET between a protein and a nucleotide (Murakoshi et al., 2004), but these approaches are limited in scope. Using fluorescence fluctuation increase by contact

(FLINC), protein activity was visualized at ~100 nm resolution (Mo et al., 2017). However, FLINC relies on the blinking statistics of the ensemble fluorescent signal, which reduces temporal resolution and does not provide information about the heterogeneous responses within the ensemble.

Here, we introduce an approach, named “binder/tag,” which is sensitive enough to report the conformational changes of individual molecules in live cells. The method is adaptable to diverse structures and requires only simple visualization of a directly excited fluorophore. As shown in Figure 1, the binder/tag approach involves a short peptide (the tag) and a small protein (the binder) that interact tightly. In the iteration addressed most extensively here, we use the 7-residue peptide SsrA that binds to the 18 kDa protein SspB with 16 nM affinity (Figure 1A) (Hersch et al., 2004; Lungu et al., 2012; Wah et al., 2002). These molecules, which mediate protein degradation in bacteria (Flynn et al., 2001; Levchenko et al., 2000), have shown no interaction with components of mammalian cells (e.g., in optogenetic studies) (Guntas et al., 2015; Lungu et al., 2012; Niopek et al., 2014). Figure 1B illustrates the binder/tag approach for proteins regulated by autoinhibition. The small peptide is embedded in the target at a position where it is exposed only when autoinhibition is released. Only in the



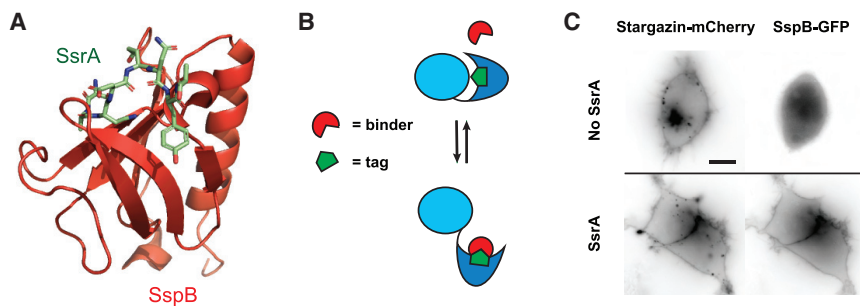


Figure 1. The binder/tag approach

(A) Crystal structure of SspB (red) and SsrA (green) in complex (PDB: 1OX9) (Song and Eck, 2003).

(B) Schematic of the binder/tag approach. A small peptide (the tag, green) is inserted where it is exposed only when the target protein is in the active conformation (here, when the dark blue autoinhibitory domain is released from the active site). When the peptide is exposed, the binder (red) can interact with the tag peptide. Tag-binder interaction is an indicator of protein activation, or a specific protein conformation. The interaction

can be detected by the localization or reduced diffusion of the binder, by colocalization, or by FRET.

(C) SspB is co-expressed with either SsrA fused to Stargazin (a transmembrane protein) or with Stargazin alone. SspB is fused to GFP, and Stargazin is fused to mCherry. SspB translocates to the membrane only when co-expressed with the Stargazin-SsrA fusion. HEK293 cells imaged with epifluorescence microscopy. Scale bar, 10 μm .

activated, uninhibited conformation can the binder interact with the target protein. Thus, target activation is reflected in the colocalization of the binder and the target or simply by arrival of fluorescent binder where nonfluorescent target protein is known to be localized. We show the proteins can be labeled either through fluorescent protein fusion or intracellularly with dyes using HaloTag or SNAP-tag.

Single particles can be tracked in 3D. However, we restrict ourselves to total internal reflection (TIRF) microscopy for validation of the technique with high resolution. We focus on Src kinase, whose effects are controlled by localized activation (Boggon and Eck, 2004; Parsons and Parsons, 1997; Summy and Gallick, 2003; Thomas and Brugge, 1997). Src family kinases (SFK) are regulated by SH2 and SH3 autoinhibitory domains (AID) that bind and inactivate a kinase domain (Boggon and Eck, 2004; Roskoski, 2004, 2015). Our studies focus on Src at integrin-based adhesion complexes, where Src is at the intersection of several signaling pathways (Brown and Cooper, 1996; Huveneers and Danen, 2009; Parsons and Parsons, 2004; Sato et al., 2009; Thomas and Brugge, 1997; Yeatman, 2004).

We used binder/tag to study Src activation kinetics and nanoscale organization. Both activation and concentration of Src increased with adhesion size. At the plasma membrane, Src was in nanoscale clusters containing a subcluster of activated slow-diffusing molecules. Computational analysis of SPT data allowed us to infer the kinetics of Src activation/inactivation at nanoscale clusters in live cells. We also showed applicability to the kinases Fyn, Syk, and FAK, and characterized an orthogonal binder/tag pair (ePDZ/ARVCF).

RESULTS

Conformation-dependent interaction of the binder with proteins bearing the tag peptide

As “binder” and “tag” we used stringent starvation protein B (SspB, 18 kDa, the binder), and the seven-residue SsrA peptide from *Haemophilus influenzae* (the tag), which bind with 16 nM K_d (Hersch et al., 2004; Lungu et al., 2012; Wah et al., 2002). The small SsrA peptide could be inserted into target proteins where its interactions with SspB depended on protein conformation and minimally affected protein function. Published BLAST ana-

lyses and imaging studies indicated that SsrA and SspB do not interact with components of mammalian cells (Lungu et al., 2012; Niopek et al., 2014).

We first verified that SspB could bind SsrA in cells. SspB was co-expressed either with the transmembrane protein Stargazin (Letts et al., 1998) or with Stargazin fused to SsrA. In each case, SspB was labeled with GFP and Stargazin with mCherry. Wild-type Stargazin produced a diffuse cytoplasmic SspB localization, whereas Stargazin-SsrA clearly recruited SspB to the plasma membrane, indicating binding of SspB to SsrA (Figure 1C).

Next, we tested whether we could place SsrA in Src at a position where SspB binding would be affected by Src conformation. Src is regulated by its SH2 and SH3 autoinhibitory domains, which bind and inactivate the kinase domain. We screened SsrA insertion sites at the interface between the AID and kinase domain, where SsrA would be shielded from SspB only in the closed, inhibited conformation (Figure 2A, sites 1–4). We also examined insertion at the C terminus (Figure 2A, sites 5–8), where the closed conformation could prevent interactions with SspB, but where peptide insertion would likely not affect normal ligand interactions. Each insertion site was evaluated for conformation-dependent SspB binding and for perturbation of normal regulation. In LinXE cells transfected with Src SsrA insertions, we used phosphotyrosine blots (Figure 2B) and pull-down assays (Figure 2C), comparing open conformation Src (Figures 2B, Y527F, and 2C, Y527F/D388R) and wild-type Src. SsrA inserted after residue N535 at the C terminus (site 7) produced conformation-dependent interactions and maintained normal regulation (Figure 2A). Published crystal structures showed that SspB bound to this site was unlikely to affect Src interactions with regulatory or effector proteins (Figure 2D). For the biological applications below, we focused exclusively on SsrA inserted after N535, which we named tagSrc.

To test whether binder and tagSrc interacted in live cells, we co-expressed SspB-mCherry with constitutively active tagSrc-GFP in HeLa cells (Figure 2E). SspB showed co-localization with tagSrc near the nucleus, where Src is known to accumulate (Chu et al., 2014; Fincham et al., 1999; Sandilands et al., 2004). In contrast, SspB was uniformly localized in cells that did not express tagSrc.

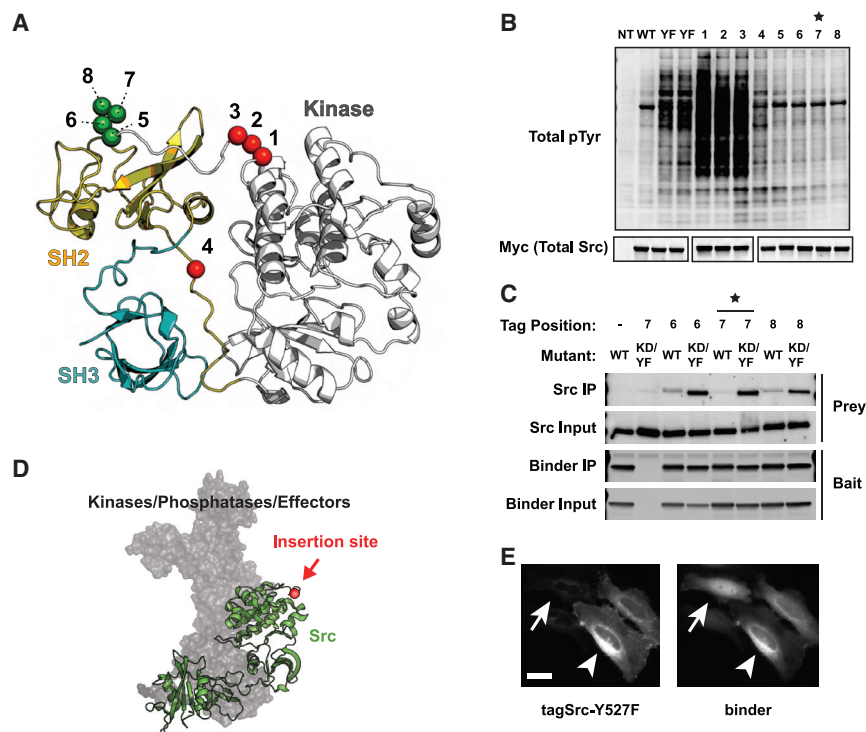


Figure 2. Identification and validation of a peptide insertion site for Src

(A) Crystal structure of Src with the tested insertion sites shown as color-coded spheres. Color indicates whether SsrA insertion resulted in either conformation-dependent binding of SspB and normal kinase regulation (green), or resulted in constitutively active kinase (red). Kinase domain (gray), SH2 (yellow), and SH3 (cyan).

(B) LinXE cells were transfected with different Src constructs and whole-cell lysates were immunoblotted for the indicated proteins. Non-transfected (NT), wild-type (WT), and Src active mutant (Y527F, or YF) are shown as controls. Numbered lanes correspond to the different SsrA-insertion sites as shown in (A). Site 7 (star) was selected as optimal. Blot representative of three independent replicates.

(C) Comparing SspB interaction with wild-type tagSrc (WT) versus tagSrc open mutant (Y527F/D388R, or KD/YF). The tag was inserted at the indicated positions (top), as shown in (A). Co-immunoprecipitation of Src-SsrA and FLAG-SspB (binder). Blot representative of three independent replicates. KD, kinase-dead.

(D) Crystal structure of Src (green; PBD: 1Y57) (Cowan-Jacob et al., 2005) showing optimized peptide insertion site (red) and interacting proteins (gray surface). Interacting proteins are Csk (PBD: 1K9A) (Ogawa et al., 2002), Cbl-c (PBD: 3VR0)

(Takeshita et al., 2012), PTPN-22 (PBD: 3BRH), and p130cas (PBD: 1X27) (Nasertorabi et al., 2006).

(E) HeLa cells co-transfected with SspB-mCherry and an open mutant of tagSrc-GFP (Y527F). Cells were imaged using epifluorescence microscopy. Full arrow indicates low tagSrc-expressing cells; arrowhead indicates high tagSrc-expressing cells. SspB colocalizes with tagSrc, and is uniformly distributed without tagSrc. Scale bar, 10 μ m.

See also Figure S1.

The Src family kinase Fyn shares extensive structure and sequence homology with Src but regulates distinct cellular processes (Chu et al., 2014; Mkaddem et al., 2017; Palacios and Weiss, 2004; Sandilands et al., 2007). We tested whether insertion of SsrA into Fyn at the same site used for tagSrc could produce conformation-dependent binding of SspB. Similar to tagSrc, in immunoprecipitation assays the open conformation of Fyn (Y527F/K299M) pulled down more SspB than did wild-type Fyn (Figure S1A). Either of the two insertion sites that we tested could be used. We also tested whether a binder/tag analog could be made from a protein with different regulatory domains than Src and Fyn. Syk kinase bears two SH2 domains that suppress activity in the resting state (Figure S1B) (Tsang et al., 2008). We engineered selective SspB binding to Syk's active conformation by screening tag sites at the interface between the AID and kinase domains. Syk with SsrA after residue N11 bound SspB only in the active state (Figure S1C). Phosphotyrosine blots indicated that this tagSyk was functional and regulated normally (Figure S1D). When the subcellular localization of a target protein is readily apparent, simple fluorescence imaging can be used to assess tag insertion sites, as we demonstrated using the adhesion localization of focal adhesion kinase (FAK) (Figures S1E–S1G).

Identifying an alternative peptide-protein pair could enable simultaneous study of two proteins or two different protein sites in the same cell. We therefore replaced SsrA with ARVCF peptide, which binds to ePDZ with high affinity (Figure S1H) (Laura

et al., 2002). Pulldown experiments showed that ePDZ bound selectively to the open conformation mutant of ARVCF-tagged Src (Y527F/D388R) (Figure S1I).

Visualizing Src Activation with binder/tag FRET—Optimizing binder and tag affinity

Although our focus was on imaging conformational changes of single molecules, we tested whether binder/tag could also provide a route to FRET biosensors (Figure 3A). Binder/tag could be used to apply FRET to targets otherwise difficult to engineer. Due to the high affinity of binder and tag, we were concerned that binder could interact with tag peptide exposed briefly during normal molecular motions of the inactive conformation, shifting the equilibrium toward activation. Dual chain biosensor designs based on intermolecular FRET have used affinities of 200–600 nM (Gulyani et al., 2011; Nalbant et al., 2004), whereas the K_d for binder and tag is below 20 nM (Hersch et al., 2004; Lungu et al., 2012; Wah et al., 2002). To test for binder-induced protein activation, we titrated SspB in LinXE cells expressing tagSrc (Figure S2A). SspB expression did induce tagSrc activation in a dose-dependent manner, as indicated by increased phosphorylation of paxillin (a Src effector) at Y31 and cell rounding, a well-documented phenotype of Src hyperactivation (Fincham et al., 1999) (Figures S2B and S2C). To work at the concentrations required for sufficient FRET brightness, a reduced affinity binder/tag was needed.

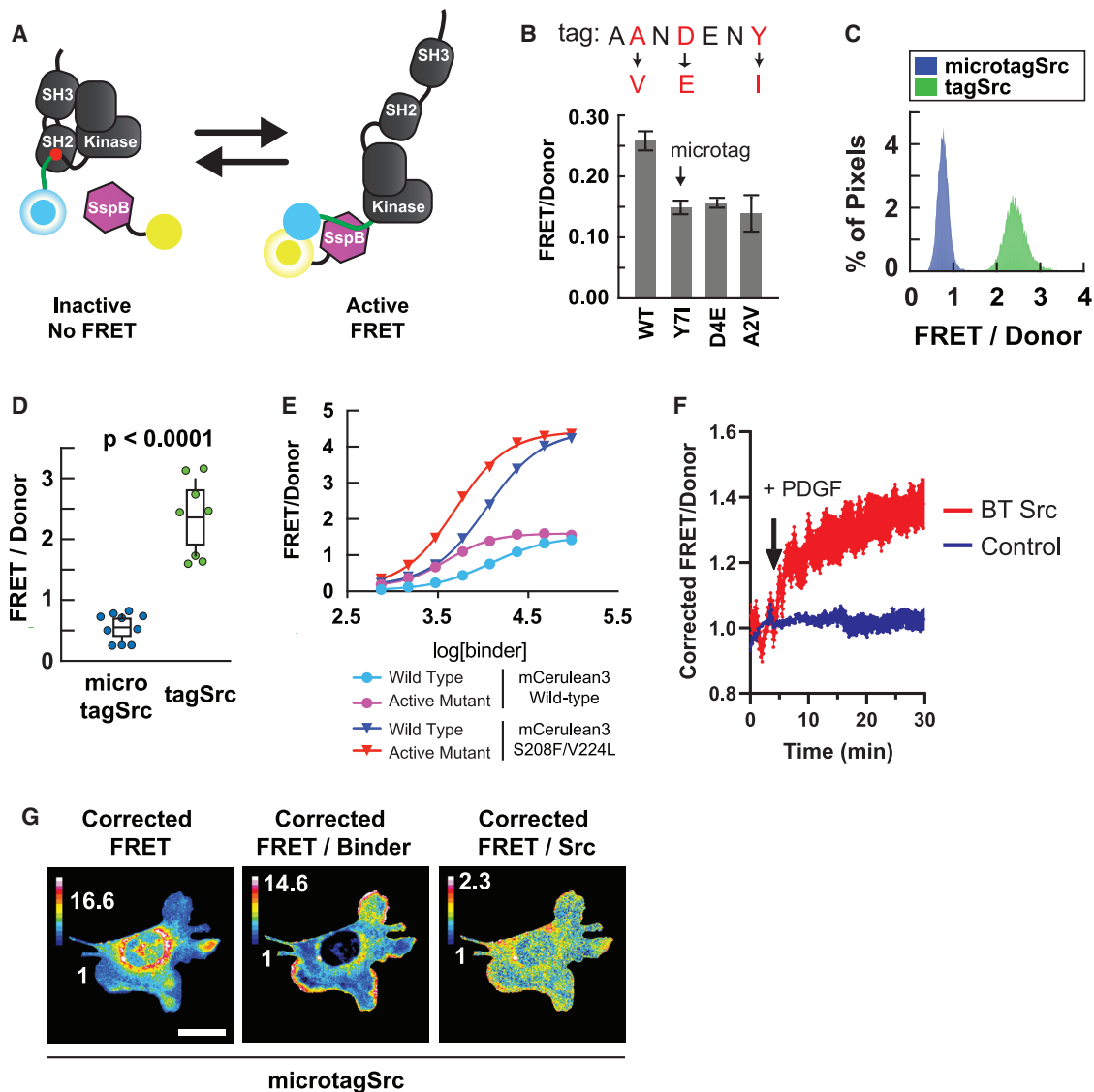


Figure 3. FRET biosensor using reduced affinity binder/tag

(A) Schematic of the binder/tag FRET biosensor. Blue, donor; yellow, acceptor; green, SsrA.

(B) Initial screen to identify tag mutants with reduced affinity. Normalized FRET/CFP emission values for LinXE cells expressing the tagSrc FRET biosensor with the indicated tag mutants are shown. TagSrc and SspB were expressed at approximately equal levels as measured by average CFP and YFP emission intensities. Measurements of selected mutants from Figure S2G were replicated. Error bars are 95% confidence intervals (n = 4).

(C) Histogram of FRET/CFP emission values for MEF cells expressing Src FRET biosensors using either tagSrc or micro-tagSrc.

(D) FRET/CFP emission values for MEF cells expressing Src FRET biosensors using either micro-tagSrc (n = 10) or tagSrc (n = 8). p value was calculated with an unpaired two-sample Student's t test. Tukey box-and-whisker plot shown with all data points displayed as dots.

(E) High-content live cell imaging of LinXE cells expressing tagSrc FRET biosensors with and without mutations that enhance Cerulean-YFP binding. SspB was titrated against a constant tagSrc concentration.

(F) Corrected FRET/tagSrc fluorescence ratios during PDGF stimulation of LINXE cells expressing either the tagSrc FRET biosensor or tagSrc-mCerulean with yPet-cp229 (no SspB). PDGF (50 ng/mL) was added at 5 min. Intensity was integrated for multiple cells in each 10× field of view. tagSrc, n = 7 fields of view; control, n = 5 fields of view; each from two independent experiments. Shown as mean ± SEM.

(G) MEF cells expressing the micro-tagSrc FRET biosensor. Micro-tagSrc and SspB were expressed at approximately equal levels as measured by CFP and YFP emission intensities per unit area. Color scales indicate bleedthrough-corrected FRET emission (distribution of active molecules, left), bleed-through corrected FRET/YFP emission ratio (distribution of active molecules corrected for cell volume, middle), or bleedthrough-corrected FRET/CFP emission ratio (activation per unit Src, right).

See also Video S1.

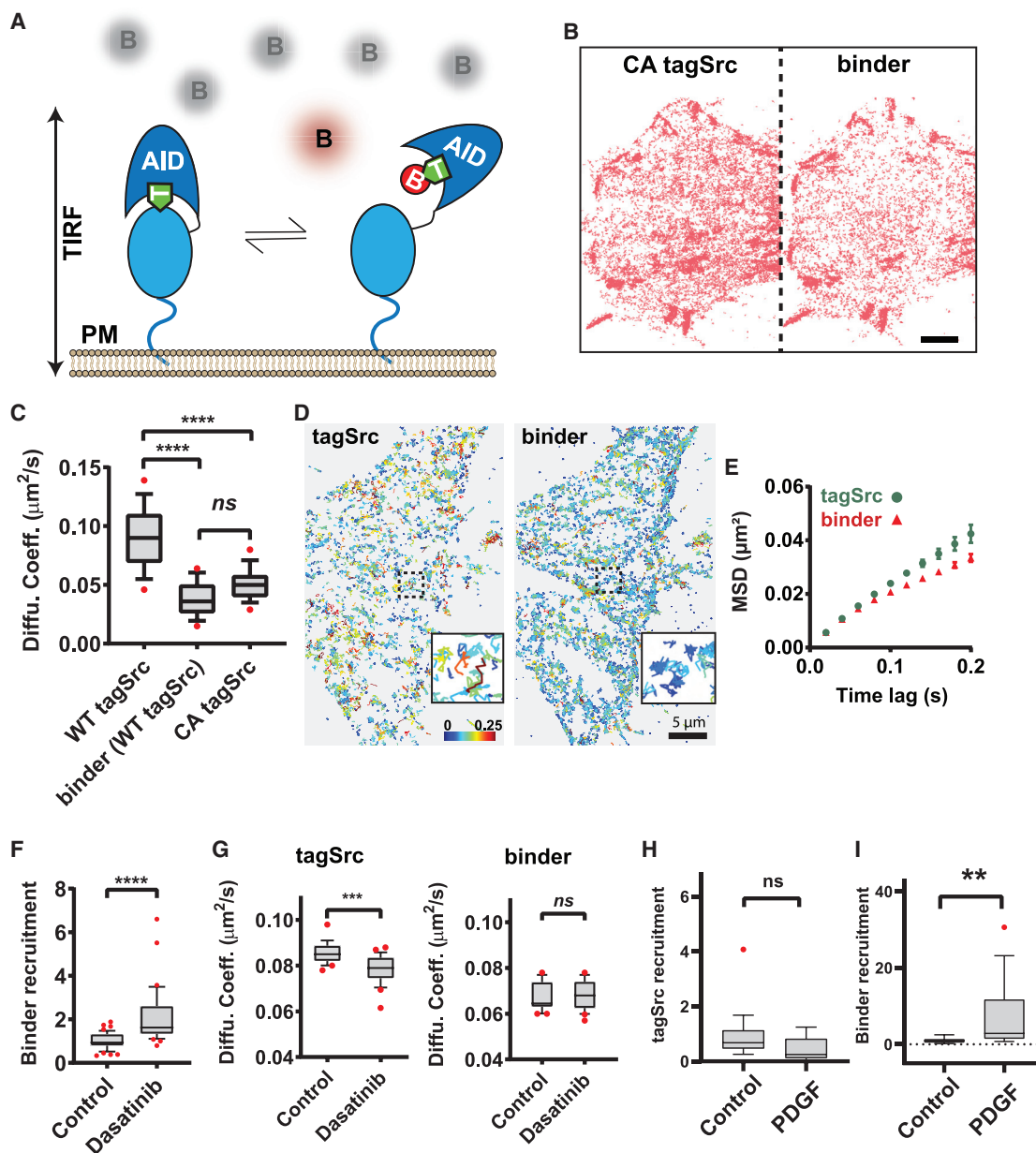


Figure 4. Using binder/tag to probe conformational states during single particle tracking

(A) Reporting the conformational states of single molecules in cells with binder/tag (T, tag; B, binder; AID, auto-inhibitory domain; PM, plasma membrane; and TIRF, total internal reflection fluorescence). Binder is observed only when it is bound to the tag embedded in the target protein. The tag is exposed in the active conformation, when the AID is not bound to the active site.

(B) Single particle tracking of constitutively active tagSrc (CA tagSrc-yPet, left) and binder (binder-PATagRFP, right) in transiently transfected COS-7 cells. Scale bar, 10 μm .

(C) Diffusion coefficients obtained by mean-squared displacement (MSD) analysis for wild-type tagSrc-yPet (left, $n = 18$ cells), binder-PATagRFP co-expressed with wild-type tagSrc-yPet (middle, $n = 18$ cells), and constitutively active tagSrc-yPet (right, $n = 15$ cells). Box-and-whisker plot shown with outliers displayed as dots. Significance judged by one-way ANOVA, **** $p < 0.0001$ with Tukey-Kramer correction for multiple hypotheses.

(D) Single particle tracking of tagSrc-Halo and binder-SNAP, labeled with JF646 and JF549 respectively, in BT-MEF cells. Trajectories are colored to indicate diffusion coefficients ($\mu\text{m}^2/\text{s}$).

(E) MSD analysis of tracks shown in (D). Data shown as mean \pm SD.

(F) Binder recruitment responds to the Src inhibitor dasatinib (tracks/ μm^2 /frame). Box-and-whisker plots show outliers as dots. Control, $n = 46$ cells; dasatinib, $n = 32$ cells. Significance judged by unpaired two-tailed Student's t test, **** $p < 0.0001$.

(legend continued on next page)

We used FRET between binder and tagSrc to assay the effects of SsrA point mutations on affinity. First, FRET efficiency was optimized by screening variants of yellow fluorescent protein (YFP) and cyan fluorescent protein (CFP), attached to constitutively active tagSrc (CA tagSrc) and SspB, respectively (Figure S2D). The variants differed in quantum yield, extinction coefficient, and propensity to dimerize. We also examined circular permutants to optimize fluorophore orientation. Based on all these studies, mCerulean3 and yPet circularly permuted at residue 229 were chosen as the optimal FRET pair (Figure S2D, star). Although CyPet gave the highest sensitized emission, the greater brightness of mCerulean3 produced superior signal-to-noise. When the optimized proteins were expressed in mouse embryonic fibroblasts (MEF), CA tagSrc produced substantially more FRET than wild-type tagSrc (Figures S2E and S2F).

Using a high content imaging assay to quantify FRET (Slattery and Hahn, 2014), we screened point mutations of SsrA for their effects on SspB binding (Figure S2G). Mutations were selected based on a previous study of SsrA/SspB interactions (Flynn et al., 2001). The initial screen identified several mutants with reduced affinity (Figure 3B). For the following FRET biosensors, we used mutant Y7I and named Src analogs with this mutation micro-tagSrc (for micromolar affinity). The reduced affinity of micro-tagSrc was confirmed using co-immunoprecipitation (Figure S2H) and FRET in individual cells (Figure 3C and 3D). To better understand the effects of concentration on biosensor sensitivity and binder-induced tagSrc activation, we constructed a mass action model of SspB binding to SsrA-proteins (Figures S2I–S2K; STAR Methods). This confirmed that micro-tagSrc could be used to produce sufficient signal without spurious activation.

To image Src activity using a micro-tagSrc FRET biosensor, we further enhanced FRET efficiency by modifying mCerulean3 with two point mutations to promote interaction between mCerulean and yPet (S208F and V224L) (Vinkenburg et al., 2007). This “sticky” variant enhanced FRET without compromising dynamic range (Figure 3E). The optimized FRET biosensor (microtagSrc-mCerulean3-S208F/V224L with yPet-cp229) responded to platelet-derived growth factor (PDGF) stimulation (Figure 3F) and showed localized Src activity consistent with previous Src biosensors (Gulyani et al., 2011), including transient activation in protrusions and around the nucleus (Figure 3G; Video S1).

MEFs expressing tagSrc and SspB at optimized concentrations

In single particle tracking, where fluorescent molecules had to be sparse to discern individual tracks, concentration was low and there was no need to reduce SsrA/SspB affinity (see model Figure S2J). To maintain the biosensor at low concentrations, we generated MEFs stably expressing tagSrc and SspB under control of a doxycycline-inhibited promoter. TagSrc and SspB were fused to HaloTag (Los et al., 2008) and SNAP-tag (Keppler et al.,

2003) respectively, for labeling with membrane-permeable dyes that are brighter than fluorescent proteins. Successful transduction and dye attachment were confirmed by imaging (Figure S3A). Fluorescence-activated cell sorting (FACS) was used to isolate a cell population with optimal expression level and tagSrc/SspB expression ratio (Figure S3B). These cells are denoted BT MEFs. After sorting, the variability in tagSrc expression level was similar to that of endogenous Src (Figure S3C). Because expression was relatively uniform, ensemble measurements based on biochemical techniques could be used to infer properties of individual cells. Without adding doxycycline, western blotting of BT MEF lysates showed that tagSrc was ~21-fold as abundant as endogenous Src (Figure S3D). Using doxycycline to control expression, tagSrc could be tuned down to 0.2-fold endogenous Src levels (Figures S3D and S3E). Importantly, the ratio of SspB/tagSrc expression was relatively constant over the range of tagSrc expression levels we examined, ranging from 1–2 (Figure S3D).

Single molecule imaging of tagSrc was possible at all the expression levels, but visualization of SspB was difficult when doxycycline was above 100 pg/mL. To ensure that the necessary tagSrc expression levels did not affect Src regulation or downstream signaling, we assessed phosphorylation of Src (Y416 and Y527) and the Src substrate paxillin as a function of tagSrc expression (Figure S3F). Expression up to 10-fold endogenous Src did not alter Src or paxillin phosphorylation. In contrast, expression at 40-fold endogenous reduced the inactivating phosphorylation at Src Y527, increased the activating phosphorylation at Src Y416, and increased phospho-paxillin (Figure S3F). We therefore carried out all the following biological studies at <7-fold endogenous Src, with SspB at the minimum necessary expression level.

To assess whether these concentrations led SspB to activate Src, we examined Src regulatory phosphorylation. MEFs expressing high and low amounts of SspB within our optimized concentration range (Figure S3B, right panel) did not display Src phosphorylation significantly different from MEFs lacking SspB (Figure S3G). This indicated that SspB concentrations were below the threshold for appreciable binding to inactive tagSrc, and SspB was binding tagSrc activated by endogenous regulatory mechanisms.

Binder/tag reports the conformation of individual Src molecules

TIRF microscopy was used to examine the conformational state of individual Src molecules in living cells. Because TIRF selectively illuminates a region up to roughly 100 nm from the coverslip, only binder molecules captured by Src at the ventral PM were clearly visible. The small proportion of unbound binder molecules that were within TIRF illumination diffused much more rapidly than the binder captured by tagSrc (Figure 4A). We controlled fluorophore concentrations so that individual tracks

(G) Diffusion coefficients of tagSrc (left) and binder (right) in cells treated with dasatinib, obtained by MSD analysis. Box-and-whisker plots shown with outliers displayed as dots. Control, $n = 20$ cells; dasatinib, $n = 26$ cells. Significance judged by unpaired two-tailed Student's t test, *** $p < 0.001$.

(H and I) TagSrc (H) and binder (I) recruitment (tracks/ μm^2 /frame) respond to PDGF treatment (20 ng/ml for 20 min). Box-and-whisker plots show outliers as dots. Control, $n = 15$ cells; PDGF, $n = 14$ cells. Significance judged by unpaired two-tailed Student's t test, ** $p < 0.01$.

See also Figures S3 and S4.

could be discerned, using either SNAP-tag and HaloTag (Kessler et al., 2003; Los et al., 2008) or photoswitchable fluorescent proteins. SNAP-tag and HaloTag provided robust means to covalently label binder and/or tagSrc with bright Janelia Fluor dyes (Grimm et al., 2015), and the dye/protein ratio could be adjusted simply by incubating the cells with different concentrations of dye. Photoswitchable proteins could be controlled to limit the number of visible fluorophores (Shcherbakova et al., 2014).

SPT of binder expressed alone yielded very few tracks (<1 new track per frame), showing that binder had little non-specific interaction with the PM (Figures S4A, left, and S4B). Binder co-expressed with tag (SsrA) fused to the transmembrane receptor Stargazin was localized to the PM, as expected (Figure S4A, right). We further validated binder/tag by co-expressing binder with tagSrc-Y527F (constitutively active tagSrc [CA tagSrc]). The Y527F mutation reduces affinity of the C terminus for the SH2 domain, leaving Src in the open conformation (Cooper et al., 1986; Kmiecik and Shalloway, 1987; Roskoski, 2004). Dual-color SPT showed that CA tagSrc and binder produced similar track maps, indicating that binder interacted with CA tagSrc (Figure 4B). Although the maps were similar, the majority of individually tracked tagSrc and binder molecules did not co-diffuse. This was because only a fraction of the tagSrc and binder populations were fluorescent. The images from these studies suggested that CA tagSrc and binder accumulated on focal adhesions (Figure 4B), as was confirmed by colocalization with adhesion markers (see below). To test whether the binder was selectively reporting the open conformation of Src, we compared the diffusion of tagSrc, CA tagSrc, or binder with tagSrc (Figures 4C, S4C, and S4D). The diffusion coefficients of TagSrc and CA tagSrc were markedly different, likely because the open form of Src bound to immobilized or slowly diffusing ligands. When co-expressed with tagSrc, binder showed the same slower diffusion observed for CA tagSrc, indicating that binder interacted selectively with the open, active form of wild-type tagSrc. The slower diffusion of active tagSrc was consistent with prior studies using Src-Y527F (Machiyama et al., 2015; Shvartsman et al., 2007). Altogether, these results show that binder interacts selectively with the open conformation of tagSrc, and this produced clearly discernable effects on particle diffusion and localization.

We tested whether diffusion rates of tagSrc were normal under our experimental conditions. Abnormal diffusion was detected only at 10-fold endogenous levels (Figures S4E and S4F), potentially due to full saturation of slow-diffusing binding partners. At a doxycycline concentration producing 4- to 7-fold endogenous Src expression levels, there was sufficient signal from both tagSrc and binder. Neither Src diffusion nor phosphorylation of Src substrates was perturbed at up to 7-fold overexpression (Figures S3F, S4E, and S4F). Furthermore, increasing binder expression did not affect Src activation or diffusion (Figures S3G, S4E, and S4F). These conditions were used for all subsequent experiments unless otherwise noted.

Dual-color imaging of tagSrc and binder diffusion (Figures 4C–4E) showed that binder diffused more slowly than the overall tagSrc population, indicating that it was binding to activated Src. Moment scaling spectrum analysis (Ewers et al., 2005; Fer-

rari et al., 2001) revealed that Src can exist in both free and confined diffusional states (Figure S4G). Binder showed a significantly higher percentage of tracks in a confined diffusional state than did tagSrc, likely due to interactions with slow-diffusing binding partners and/or enclosure within cytoskeletal corrals (Kusumi et al., 2005). These differences between the diffusion of binder and tagSrc populations further supported the selective interaction of binder with the open form of Src.

Finally, both the activity and PM localization of Src are known to be affected by phosphorylation (Boggon and Eck, 2004; Shvartsman et al., 2007). We therefore examined the effects of dasatinib, a kinase inhibitor known to reduce Src phosphorylation at Src Y416 and Y5277 (Milano et al., 2009; Pichot et al., 2009). In our BT MEFs, dasatinib produced dose-dependent dephosphorylation (Figure S4H) of both residues and increased binder recruitment to the PM (Figure 4F). Src phosphorylation at Y527 maintains the closed conformation, and phosphorylation at Y416 increases kinase activity. Because dasatinib disrupts both of these (Li et al., 2010; Rix et al., 2007; Roskoski, 2015), it produces an open, inactive Src that can interact with binder. Even though dasatinib did not increase catalytic activity, the open Src showed reduced diffusion (Figure 4G). This indicated that kinase activity is not required for interaction of open Src with other molecules, an unappreciated ability of dasatinib to generate dominant-negative Src (Figure S4I).

Published studies (Kypta et al., 1990) and our experiments with binder/tag FRET above showed that Src is activated when cells are stimulated with PDGF (Figure 3F). SPT of binder/tag Src revealed that this was primarily due to activation of membrane-resident Src rather than translocation of activated Src to the membrane (Figures 4H and 4I).

Src recruitment, concentration, and activation at adhesions

We used binder/tag first to corroborate biosensor studies showing Src activity at adhesions (Koudelková et al., 2019; Lu et al., 2014) and to ask how Src activation is affected by adhesion maturation. We obtained snapshots of adhesion markers every minute and in between performed dual-color SPT of binder and tagSrc in 20-s blocks (Figures 5A and 5B). To identify adhesions, we used fluorescently labeled paxillin-EGFP because paxillin is present from the beginning of adhesion formation (Gardel et al., 2010). At the concentrations of paxillin-EGFP used, neither adhesion morphology (Figure S5A), the diffusion of tagSrc, nor the diffusion of binder (Figure S5B) was affected.

Although tagSrc diffused more rapidly outside adhesions (Figure 5C), binder was slow diffusing regardless of localization, consistent with binder interacting selectively with activated Src, bound to other proteins. Src is known to be involved in adhesion maturation (Gardel et al., 2010; Huvneers and Danen, 2009; Webb et al., 2004). Adhesions enlarge as they mature (Chu et al., 2014; Karginov et al., 2014; Koudelková et al., 2019; Playford and Schaller, 2004), so we asked whether Src behavior correlated with adhesion size. Adhesions were binned into small (0.05–0.25 μm^2), medium (0.25–1 μm^2), and large (1–5 μm^2) categories, based on previously described sizes of nascent adhesions, focal complexes, and focal adhesions (Gardel et al., 2010; Han et al., 2015). The tracks inside and outside

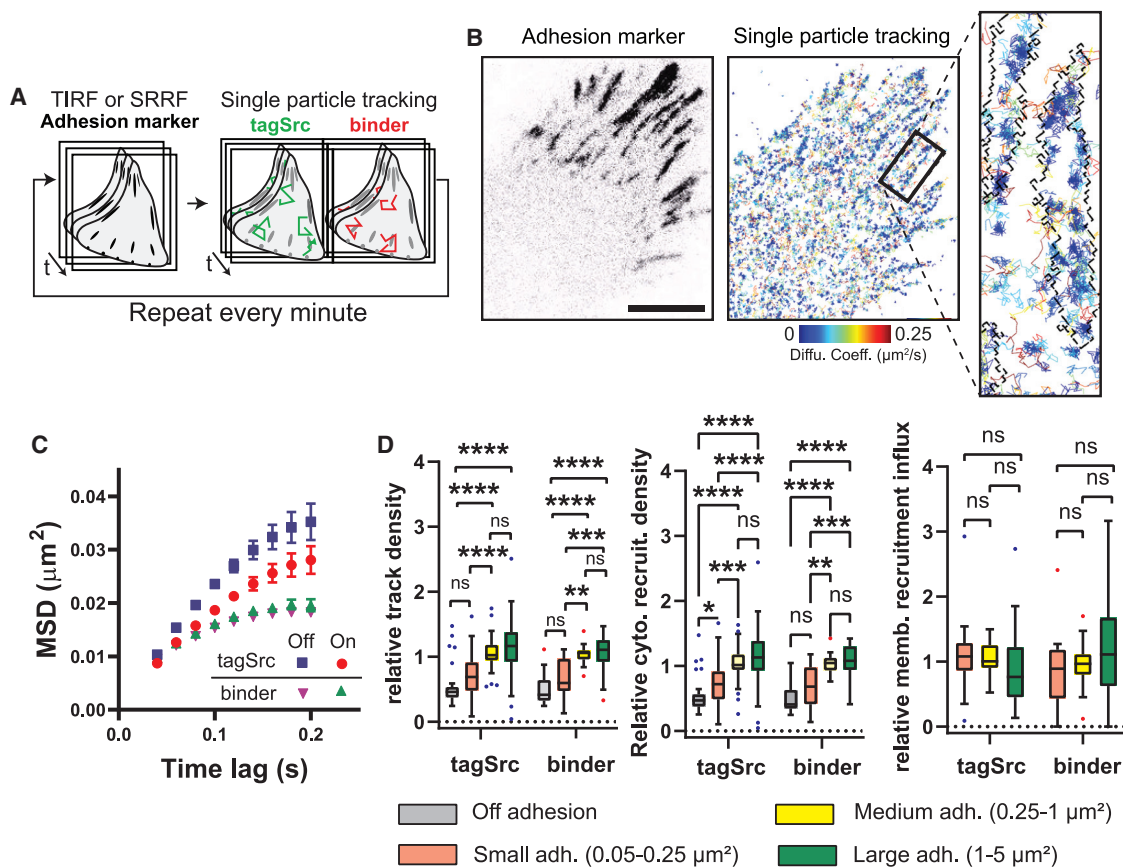


Figure 5. Correlating adhesion imaging and binder/tag single particle tracking to study Src recruitment and activation at adhesions

(A) Experimental approach. To correlate adhesions with tagSrc and binder tracks, adhesion markers were imaged every minute, either by TIRF (B, Figures S5D and S5E) or for 2 s at 100 Hz for SRRF analysis (D); dual color single particle tracking of tagSrc and binder were carried out afterward.

(B) Correlated adhesion and single particle tracking maps showed clusters of tagSrc and elevated tagSrc concentration within adhesions. Adhesions occur predominantly at cell extensions in these cells. Scale bar, 10 μm .

(C) MSD analysis of tagSrc and binder tracks on and off adhesions. Error bars show SEM, $n = 16$ cells.

(D) Src activity and recruitment as a function of adhesion size. Track density was computed as the number of track centroids per unit adhesion area (left). Cytoplasmic recruitment density was computed as the number of track starts per unit adhesion area (middle). Membrane recruitment influx was computed as the number of tracks that entered adhesions by lateral diffusion per unit adhesion perimeter (right). For all quantities, “relative” denotes normalization to the average across all adhesions. Both the track density and the cytoplasmic recruitment density increased with adhesion size, for both tagSrc and binder. Adhesions were identified by super resolution SRRF imaging. Bars show mean ± 1 SD. Significance judged by one-way ANOVA, * $p < 0.05$, ** $p < 0.01$, *** $p < 0.001$, **** $p < 0.0001$ with Tukey-Kramer correction for multiple hypotheses. Data represent $n = 20$ cells.

adhesions persisted for the same length of time (Figure S5C), so track densities were used as a reasonable proxy for tagSrc and binder concentrations. Both Src and active Src concentrations increased with adhesion size, with small adhesions showing concentrations similar to those in the PM (Figures 5D, left, and S5D, left) and large adhesions having twice that concentration.

We asked whether Src was recruited to adhesions from the PM or the cytosol and whether this was a function of adhesion size. Larger adhesions recruited more cytoplasmic tagSrc per unit area (Figures 5D, middle, and S5D, middle; see also STAR Methods), but all adhesions recruited PM-associated tagSrc equally (Figures 5D, right, and S5D, middle). Thus, the greater concentration of Src in larger adhesions was due to their enhanced recruitment of cytosolic Src (Figure S5E). Qualitatively similar concentration and cytoplasmic recruitment behavior was

observed regardless of the adhesion marker (FAK-EGFP and vinculin-EGFP) (Figure S5F).

Altogether, our results showed that larger adhesions recruit, concentrate, and activate Src more effectively, and this enhanced recruitment is primarily due to uptake of Src from the cytosol, not from nearby plasma membrane. Enhanced cytosolic recruitment may be due to the increased availability of Src binding sites across the surface of large adhesions.

Nanoscale clusters of Src are dynamic hotspots of activity

Studies in fixed cells have shown that several Src family kinases organize into clusters (Githaka et al., 2016; Owen et al., 2010). Few studies of Src family kinase clusters have been carried out in living cells (Rossey et al., 2013; Smith et al., 2016), and little is

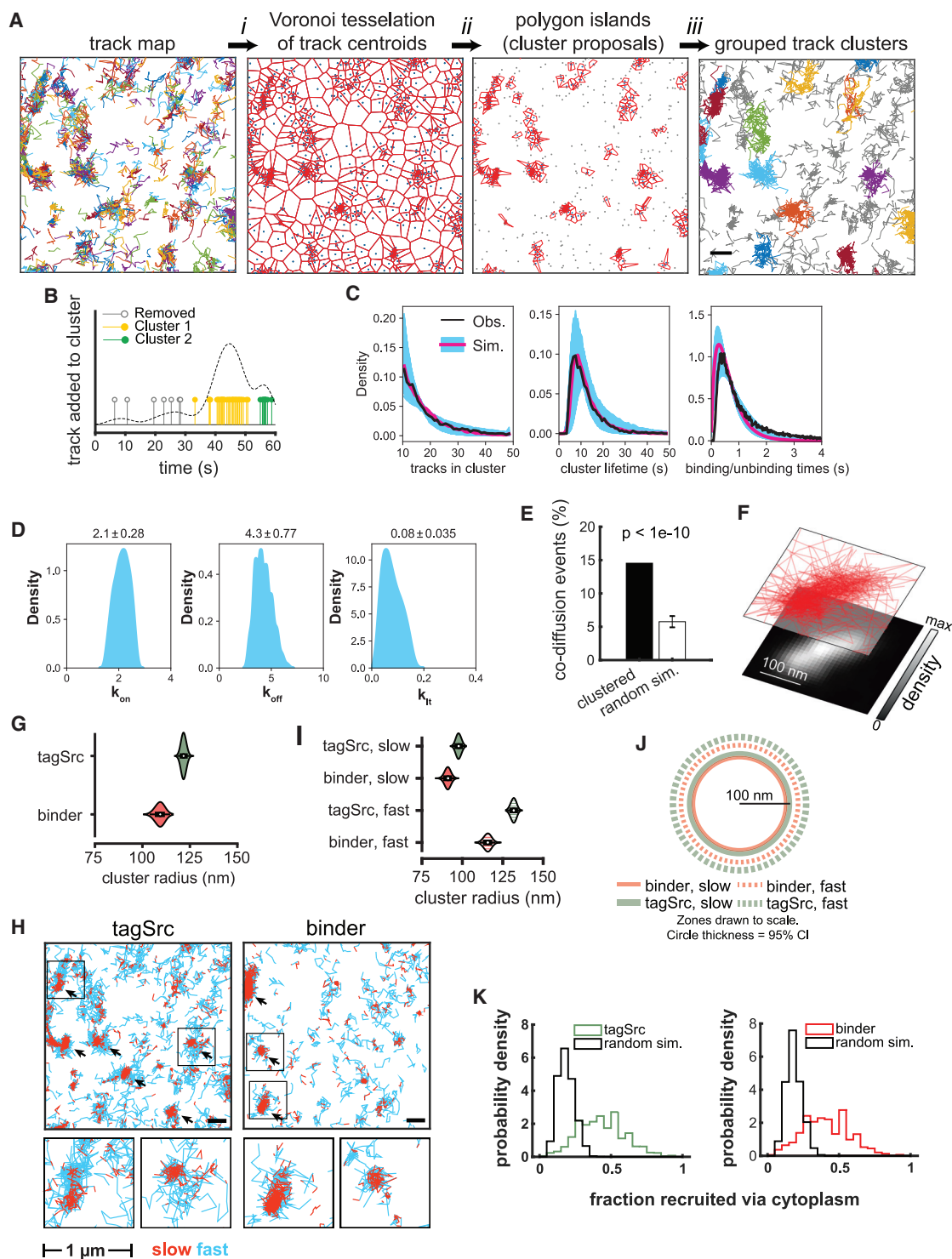


Figure 6. Src organization and activation within nanoscale clusters

(A) Workflow to identify and isolate clusters from experimental data. (i) Track maps are transformed into centroid maps and subjected to Voronoi tessellation. (ii) Large Voronoi polygons were removed, generating proposed clusters. (iii) The proposals were used to assign tracks into clusters. Scale bar, 500 nm.

(B) An example showing incorporation of temporal information in cluster detection. The temporal density is shown as a dashed black line, and the stems denote cluster classification. To be included in the same cluster requires an interval of <5 s between arrivals (STAR Methods).

(C) Distributions used in cluster kinetic analysis: number of tracks per cluster using 10 track per cluster minimum (left panel), observed lifetime of clusters containing 10 or more tracks (middle), and time interval for arrival and dissociation of labeled molecules (STAR Methods). Black curves are experimental results, (legend continued on next page)

known about Src activity within individual clusters. Therefore, we harnessed the capabilities of binder/tag to examine the dynamics of Src activation in clusters, with a resolution well beyond that of diffraction-limited live cell microscopy.

Fixed-cell photoactivation localization microscopy (PALM) imaging showed tagSrc clusters throughout the cell, not simply at adhesions, with a radius of 85 nm (Figures S6A–S6C; STAR Methods). To examine dynamic clusters, we developed an approach to identify clusters in dual color SPT imaging data from BT MEFs (Figures 6A and S6D; STAR Methods). This was based on Voronoi tessellation like that used for fixed cells (Andronov et al., 2016; Levet et al., 2015). Criteria for identifying clusters were based on both the spatial (Figure 6A) and temporal proximity (Figure 6B) of individual tracks. Other approaches have been developed for live cell single molecule cluster analyses (Griffié et al., 2018). However, because our method is based on single particle tracking data, we are able follow the behavior of individual molecules within clusters.

To obtain well-separated tracks for SPT, only a small proportion of binder or tag were dye-labeled within cells (see above). Therefore, it was rare to see two or more dye-labeled molecules in an identified cluster at any given time, opening the possibility that what we were actually observing was repeated interactions of labeled molecules with a single binding partner rather than true clusters. To determine the likelihood of such a false positive, we performed a quantitative analysis of binder/tag kinetics (STAR Methods). Our analysis demonstrated that the probability of incorrectly identifying a single binder as a cluster is exceedingly rare. The analysis also provided an estimate of 200 for the average number of Src molecules within a cluster (STAR Methods), consistent with effective radius of 85 nm estimated from PALM imaging data (STAR Methods).

We quantified cluster dynamics using a stochastic model that incorporates three kinetic steps: the association rate of tagSrc with a cluster, the disassociation rate of tagSrc from a cluster, and the disassembly rate of clusters (Figures S6F and S6G; STAR Methods). Theoretical analysis of the model demonstrated its ability to accurately reproduce experimental results for the number of labeled TagSrc tracks per cluster, the observed cluster lifetimes, and binding/unbinding events (Figures 6C and S6H). Because the model contained only 3 parameters, we also performed a systematic search of parameter space (Figures

6D and S6I), allowing us to estimate the median cluster lifetime as $T_{it} = 8.7$ s.

We wondered whether clusters were enriched in activated Src. Of all identified co-diffusion events ($n = 1,094$), 15% were in clusters (Figure 6E). Comparing this percentage with that of an *in silico* randomization control (STAR Methods), we estimate that Src molecules in clusters are 3 times more likely to be active compared to unclustered molecules.

We next examined the dimensions of clusters and the distribution of active Src within them. Cluster size was determined by creating density maps from track coordinates (Figure 6F) then defining the cluster as the region with greater than half-maximal density. This analysis produced median radii of 120–124 nm for tagSrc and 105–113 nm for binder (Figure 6G). This size difference indicated that Src activation occurs in distinct regions within larger clusters and/or that active and inactive Src are in clusters of different sizes.

Support for “islands” of active Src within clusters was provided by assigning each displacement along each track into a slow or fast diffusional state (Persson et al., 2013). This clearly revealed that both tagSrc and binder were separated into slow and fast diffusion zones within the same cluster (Figures 6H and S6K). We compared the slow and fast diffusion of tagSrc in clusters containing primarily tagSrc and the diffusion of binder in clusters containing primarily binder (Figures 6I, 6J, S6L, and S6M). As illustrated in Figure 6J, the slowly diffusing regions within tagSrc and binder clusters were roughly the same size, whereas the fast-diffusing zones were larger and varied more in average size. These data suggested that active Src within clusters is separated into a smaller slow-moving zone, and enabled us to determine the average size of each species’ distribution within clusters (median radii: 96–100 nm for slow tagSrc, 88–94 nm for slow binder, 129–134 nm for fast tagSrc, and 112–119 nm for fast binder, 95% confidence interval [CI]). Control experiments were performed to ensure that the differences were not due to analytical or experimental artifacts (Figures S6N and S6O).

We estimated that, on average, 65% of the tracks entered clusters via diffusion in the membrane. After removing tracks that diffused in from the outside (Figure S6P), the fast zone remained larger than the slow zone, demonstrating that this fast zone resulted from tracks that are diffusing away from the cluster

blue shading shows spread of results using best-fitting parameters (top 5th percentile) after a systematic parameter sweep, and the red line illustrates a specific fit ($k_{on} = 2.2 \text{ s}^{-1}$, $k_{off} = 5.1 \text{ s}^{-1}$, $k_{it} = 0.049 \text{ s}^{-1}$).

(D) Distributions of best-fit parameters, along with mean ± 1 SD. k_{on} , tagSrc association rate with a cluster; k_{off} , tagSrc disassociation rate from a cluster; k_{it} , the disassembly rate of clusters.

(E) Co-diffusion events were over-represented in clusters compared to simulated random controls. Significance determined by comparing 10 simulations against the measured value, using a one-sample Student’s t test.

(F) Example density map for a cluster, calculated using all associated track coordinates.

(G) Cluster sizes for tagSrc and binder. Distributions represent bootstrapped medians after thresholding clusters at 50% maximum density (see Figure S6J).

(H) Cluster substructure identified by a hidden Markov model-based diffusional analysis (see Figure S6K). Four example clusters highlighted, two each for tagSrc and binder, highlighting core zones of slowed diffusion.

(I) Cluster sizes for the slow and fast zones within tagSrc and binder clusters. Distributions represent bootstrapped medians after thresholding clusters at 50% maximum density (see Figure S6M).

(J) Schematic for cluster substructure based on the 95% confidence intervals in (G). Zones are drawn to scale, and the thickness of the circles corresponds to the 95% confidence interval.

(K) Measured recruitment from cytosol into clusters versus simulated random controls. All data represent $n = 61$ cells, with $n = 3,972$ tagSrc clusters and $n = 2,058$ binder clusters.

center, not from active Src entering the cluster from outside. Computer simulations predicted that 15% of tracks would arrive from the cytosol compared to the 35% observed experimentally (Figure 6K). This suggested that clusters of active Src are formed by recruitment of Src to a concentration of slow-diffusing binding sites. Finally, we note that clustered tracks had longer lifetimes than non-clustered tracks (Figure S6Q), consistent with the existence of PM-anchored binding sites.

In summary, we found that Src clusters have an effective radius of ~ 100 nm, consist of roughly 200 molecules, have a lifetime of around 9 s, and are enriched in active Src. Although most Src (65%) enter clusters via lateral diffusion, the cluster area does show an elevated ability to directly recruit Src from the cytoplasm. Within clusters, we identified zones of slow-diffusing, active Src embedded in larger zones of fast diffusing Src and provide evidence that the active molecules are produced predominantly at sites within the clusters.

Inferring *in vivo* Src kinetics

Src conformational changes have been the subject of considerable kinetic and thermodynamic analyses *in vitro* (de Mol et al., 2005; Ladbury and Arold, 2011; Payne et al., 1993; Le Roux et al., 2016) but *in vivo* measurements have not been performed. Therefore, we extended our stochastic model to study the kinetics of Src activation inside live cells. Our analyses relied on co-diffusing pairs of tagSrc and binder tracks (Figure 7A; Videos S2 and S3), which contain dynamic information about Src regulation. Src molecules at the membrane can undergo 4 kinetic steps: (1) activation (k_1), (2) deactivation (k_2), (3) release from the plasma membrane in the inactive form (k_7), and (4) release in the active form (k_8) (Figures 7B and 7C). The model also accounted for SsrA/SspB interactions (k_3 and k_4) (Figure 7D; STAR Methods).

Motivated by our competitive binding studies (Figures 3D and 3F), we considered two additional steps to account for potential effects of Src-binder interaction. We considered Src activation induced by binder (k_5) and binder dissociation caused by Src deactivation (k_6). Under our experimental conditions, binder activation of Src is negligible (Figures S3G and S7A), so we set the rate constant for this process k_5 to zero. The rate of spontaneous binder dissociation, from either tagStargazin or from tagSrc-Y527F, was slower than the observed rate of tagSrc-binder dissociation in co-diffusion events ($k_{\text{spont}} = 0.6\sim 1.3$ s $^{-1}$, $k_{\text{obs}} = 4.25$ s $^{-1}$) (Figures S7B and S7C). We therefore included k_6 as a free parameter in the model. The rate of tagSrc-binder association estimated from our cluster kinetics analysis was very low ($k_{\text{on}_b} = 0.004$ s $^{-1}$), in part due to the low dye-labeling frequency. However, if we look at the distribution of times for this process (Figure 7F, process (i)), the rate appears much higher. The reason for this discrepancy is that selecting for rare co-diffusion events produces a higher effective association rate, because association must occur before tagSrc dissociates from the PM (STAR Methods). Therefore, the effective binding rate is determined by the tagSrc dissociation rate of 3.47 s $^{-1}$. These considerations illustrate the problem with attempting to estimate single rate constants directly from the distributions shown in Figure 7F. That is, there are multiple competing transitions for each biochemical state in the Markov model, so the measured distributions do not purely represent the transitions shown in Fig-

ure 7B. To overcome this problem, the model was fit to all the data simultaneously. Photobleaching kinetics were excluded from the model because the track lifetimes were shown to be robust to increases in laser power (Figure S7C).

The model was simulated using each of the three PM-associated states as initial conditions. To simultaneously fit the model to all the experimental data, we used a two-step parameterization approach; an evolutionary algorithm (Fortin et al., 2012) provided a coarse-grained search of parameter space, after which Markov chain Monte Carlo sampling (Haario et al., 2006; Miles, 2019) was used to refine the search and construct distributions for the model parameters. We validated this approach using simulated data as the ground truth (Figures S7D and S7E). After fitting to experimental data, we obtained the parameter values and bounds shown in Figures 7E and S7F and simulation results shown in Figures 7F–7H.

Overall, the fitted model was in agreement with the SPT data. Encouragingly, the model predicts that the plasma membrane dissociation for active Src ($k_8 = 0.18 \pm 0.44$ s $^{-1}$) is much slower than that for inactive Src ($k_7 = 10 \pm 2.8$ s $^{-1}$). This result is consistent with previous observations that the open-conformation Src interacts with other proteins in the plasma membrane, whereas closed-conformation Src interacts with the plasma membrane primarily via *N*-myristoylation (Sandilands et al., 2007). The model also recapitulated several previous experimental measurements (Table S1) providing additional evidence that it captures essential features Src regulation.

In summary, through observation of binder/tag co-diffusion events and the simultaneous fitting of multiple rate parameters, we were able to determine in living cells the kinetics of Src activation, inactivation, and interaction with the plasma membrane, values that would otherwise be difficult to obtain. Our analysis provides a computational framework for examining the *in vivo* kinetics of Src and other proteins in different regions of the cell and various biological contexts.

DISCUSSION

We have described “binder/tag,” a molecular imaging approach that simplifies biosensor engineering and is sensitive enough to report the conformations of individual molecules in living cells. The method presents some clear advantages—engineering is reduced to insertion of a small peptide, this peptide can be placed where binder interactions do not compete with known ligands, and the same binder-tag pair can provide a specific interaction for many different target proteins. A potential advantage, not explored here, is the ability to replace native genes with fully functional biosensor analogs. Binder/tag should prove useful for multiplexing applications in that each activity can be visualized with a single fluorophore. For this, we validated a second, orthogonal binder/tag pair. For most biosensors one must find the intracellular concentration that provides sufficient signal/noise, but does not perturb cell biology. Binder/tag enables the use of low biosensor concentrations because it requires only detection of a directly excited fluorophore, which can be selected for brightness and photostability.

Perhaps the most challenging step in building a new binder/tag analog is finding a good insertion site for the tag. Our studies

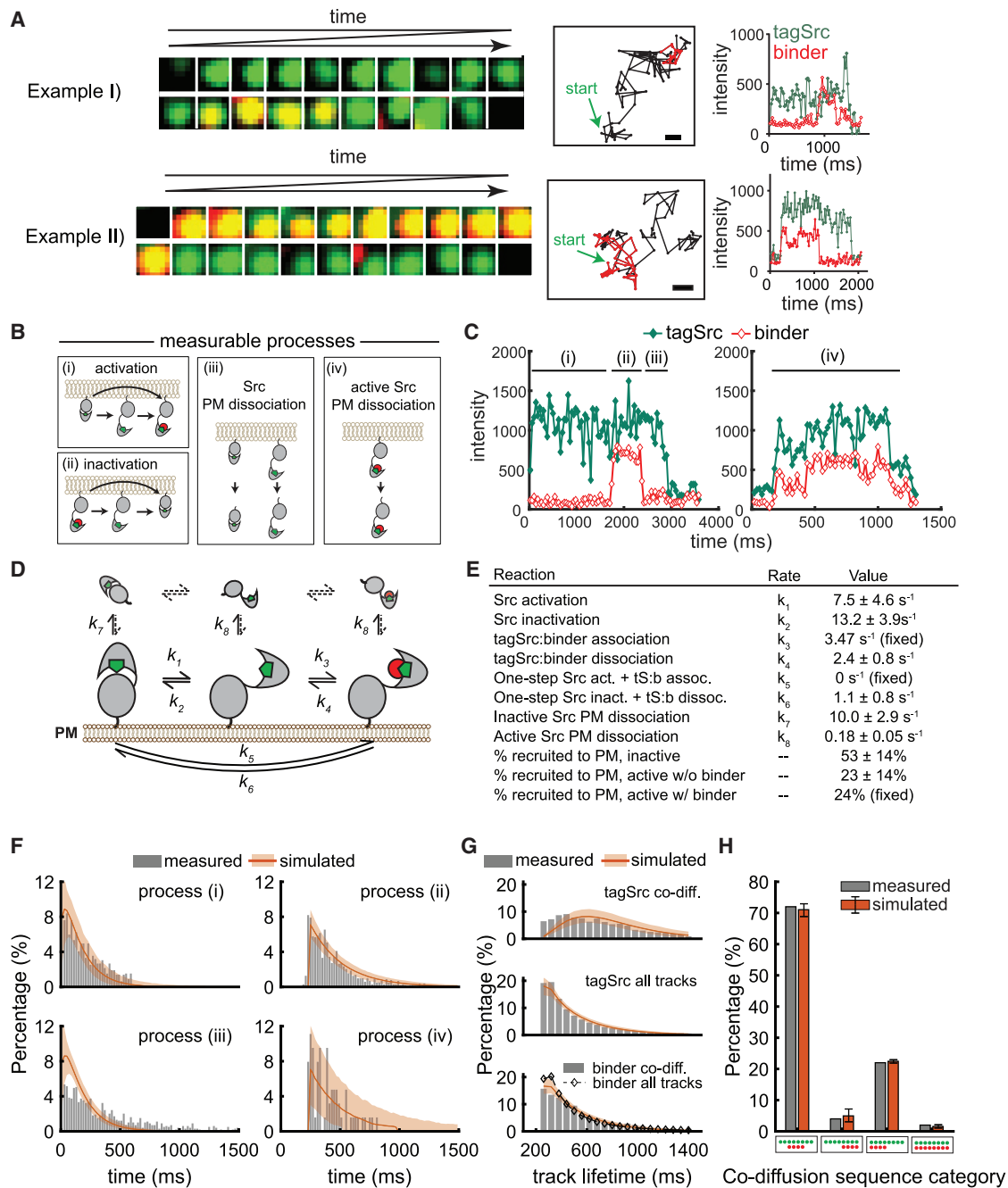


Figure 7. Measuring kinetics of Src interactions in living cells using binder/tag

(A) Two examples of co-diffusion, following tagSrc (green) and binder (red) over time (80 ms between images) (left). Example trajectories, where the tagSrc track is in black with a green arrow marking the start, and the binder track is in red (middle). Scale bar, 500 nm. The fluorescence intensities of the spots are plotted as a function of time (right).

(B) Four processes that can be measured from co-diffusion events, containing information on Src regulation.

(C) Examples of waiting times associated with the four processes.

(D) Kinetic model of tagSrc and binder. Processes corresponding to dashed arrows cannot be inferred from the data.

(E) Parameters obtained corresponding to best-fit kinetic models. Shown as mean \pm 1 SD.

(F) Simulation versus measurement for the waiting time distributions of the four processes.

(G) Simulation versus measurement for track lifetimes.

(H) Simulation versus measurement for co-diffusion sequence categories, where co-diffusion events were classified based on the order of arrivals and departures of tagSrc and binder.

Data represent $n = 1,094$ co-diffusion events identified over $n = 61$ cells. (F–H) Errors were shown as 95% confidence intervals.

See also [Figure S7](#), [Table S1](#), and [Videos S2](#) and [S3](#).

exemplify using an autoinhibitory interaction to sterically block the insertion site. Other mechanisms for conformation-dependent tag exposure can also be envisioned: Previous studies have shown large changes in the conformation of “hinge sequences” connecting autoinhibitory domains to catalytic domains upon protein activation (Azoitei et al., 2019; Marston et al., 2020). The tag peptide could be inserted in these hinges as well as on the binding interface between the AID and catalytic domain. Prior studies have shown that protein activation causes changes in surface loops that are far from the active site or important interfaces (Choi et al., 2015; Dagliyan et al., 2013, 2016; Karginov et al., 2010, 2014; Lee et al., 2008; Ostermeier, 2009). Conformational changes in such loops could affect the exposure or orientation of an inserted peptide. Success with one protein can guide insertion for whole protein families, as we did when modifying Fyn based on our success with Src.

To assess insertion sites, different assays that report protein-protein interactions could be used. We used pull-down assays (Src, Fyn, and Syk) and also simple imaging of protein localization (FAK).

The amount of binder attached to activated target proteins will be affected by the dissociation constant and intracellular concentrations of binder and the tag protein. We showed that the binder concentrations required to detect FRET with typical wide-field microscopy setups could artifactually activate the protein, so we generated a reduced affinity tag (“micro-tag”) to be used in such applications. The ability to force open target proteins could in fact be an advantage. Optogenetic analogs of binder could be used with native affinity tag for light-induced protein activation. The same protein engineering could lead to both a biosensor and an optogenetic analog.

Being able to quantify rate constants *in vivo* is invaluable. The intracellular environment can differ substantially from conditions used for *in vitro* biochemical assays, and variations across the cell can produce compartment-specific regulation of protein activity. Our results demonstrated the importance of considering all datasets simultaneously, and highlighted potential pitfalls of inferring individual rate constants from single distributions. Our computational approaches provide a mathematical foundation for future single molecule studies.

The mechanisms driving cell behavior are organized across many scales, including multimolecular systems smaller than the diffraction limit of light microscopy. We developed binder/tag to visualize dynamics of such nano-scale systems, and we provide computational techniques to quantify and interpret experimental results. We hope this integrated approach will prove valuable for investigations into spatiotemporal control of diverse proteins, and that the engineering advantages of binder/tag will provide access to previously intractable targets.

Limitations of study

One must find appropriate concentrations where spurious activation is not induced, but where the biosensor produces sufficient signal. For this, the use of tag versus microtag is important. In situations where the target protein is inaccessible to the binder, false negatives can result. Care must be taken to place the tag where binder interaction will not interfere with normal interactions of the target protein. Should this be unavoidable, it will

likely be most important to preserve upstream regulation and any downstream binding sites that contribute to localization. In many biosensors, such competitive inhibition occurs, but concentrations can be kept low to prevent dominant-negative effects.

STAR★METHODS

Detailed methods are provided in the online version of this paper and include the following:

- KEY RESOURCES TABLE
- RESOURCE AVAILABILITY
 - Lead contact
 - Materials availability
 - Data and code availability
- EXPERIMENTAL MODEL AND SUBJECT DETAILS
- METHOD DETAILS
 - Epifluorescence microscopy
 - In-cell kinase activity assay
 - Co-immunoprecipitation assay
 - Identification of effector binding sites
 - Cell rounding
 - Modeling of binding curves
 - High-content assay
 - Fluorometer assay
 - Immunofluorescence
 - PDGF treatment
 - Single molecule microscopy
 - Single molecule tracking
 - Single molecule diffusional analysis
 - Quantification of adhesion morphology
 - Quantification of FAK (or tagFAK) and binder intensity on adhesions
 - Normalized track density and track recruitment within adhesions
 - Drug treatment
 - Single molecule co-diffusion detection
 - Fixed cell PALM imaging
 - Cluster detection and analyses
 - Detecting enrichment of co-diffusion events in clusters
 - Cluster entry from cytoplasm versus plasma membrane
 - Analysis of the number of Src molecules in a cluster
 - Validation of cluster identification criterion
 - Stochastic model for cluster kinetics
 - Mathematical modeling of SPT kinetics
 - Two-step parameter inference of SPT kinetics
- QUANTIFICATION AND STATISTICAL ANALYSIS

SUPPLEMENTAL INFORMATION

Supplemental information can be found online at <https://doi.org/10.1016/j.cell.2021.09.026>.

ACKNOWLEDGMENTS

We thank Shawn Gomez and Matthew Berginski for helpful discussions regarding adhesion segmentation and Joline Tung for assistance with western blots. This work was funded by the NIH (R35GM122596 to K.M.H. and

R35GM127145 to T.C.E.). L.D.L. was supported by the Howard Hughes Medical Institute (HHMI).

AUTHOR CONTRIBUTIONS

B.L., O.J.S., and O.D. carried out the majority of the experiments. A.T.N. and B.L. contributed the work on FAK. B.L., J.C.H., and M.P. analyzed the single molecule tracking data and performed computational modeling using analytical methods from M.P. and T.C.E. L.D.L. and J.B.G. contributed fluorescent dyes and advice regarding their use. K.M.H. initiated and supervised the development of binder/tag. T.C.E. initiated and supervised the development of analytical approaches, modeling, and quantitative data analysis. B.L., O.J.S., M.P., T.C.E., and K.M.H. wrote the manuscript with input from all authors. All authors contributed to the intellectual direction of the project.

DECLARATION OF INTERESTS

The authors declare no competing interests.

INCLUSION AND DIVERSITY

One or more of the authors of this paper self-identifies as a member of the LGBTQ+ community.

Received: September 4, 2020

Revised: July 22, 2021

Accepted: September 17, 2021

Published: October 11, 2021

REFERENCES

- Andronov, L., Orlov, I., Lutz, Y., Vonesch, J.-L., and Klaholz, B.P. (2016). ClusterViSu, a method for clustering of protein complexes by Voronoi tessellation in super-resolution microscopy. *Sci. Rep.* **6**, 24084.
- Azoitei, M.L., Noh, J., Marston, D.J., Roudot, P., Marshall, C.B., Daugird, T.A., Lisanza, S.L., Sandi, M.-J., Ikura, M., Sondek, J., et al. (2019). Spatiotemporal dynamics of GEF-H1 activation controlled by microtubule- and Src-mediated pathways. *J. Cell Biol.* **218**, 3077–3097.
- Berginski, M.E., Vitriol, E.A., Hahn, K.M., and Gomez, S.M. (2011). High-resolution quantification of focal adhesion spatiotemporal dynamics in living cells. *PLoS ONE* **6**, e22025.
- Boggon, T.J., and Eck, M.J. (2004). Structure and regulation of Src family kinases. *Oncogene* **23**, 7918–7927.
- Bowman, A.W., and Azzalini, A. (1997). *Applied Smoothing Techniques for Data Analysis* (Oxford University Press Inc.).
- Brown, M.T., and Cooper, J.A. (1996). Regulation, substrates and functions of src. *Biochim. Biophys. Acta* **1287**, 121–149.
- Choi, J.H., Laurent, A.H., Hilsner, V.J., and Ostermeier, M. (2015). Design of protein switches based on an ensemble model of allostery. *Nat. Commun.* **6**, 6968.
- Chu, P.-H., Tsygankov, D., Berginski, M.E., Dagliyan, O., Gomez, S.M., Elston, T.C., Karginov, A.V., and Hahn, K.M. (2014). Engineered kinase activation reveals unique morphodynamic phenotypes and associated trafficking for Src family isoforms. *Proc. Natl. Acad. Sci. USA* **111**, 12420–12425.
- Colquhoun, D. (2007). Why the Schild method is better than Schild realised. *Trends Pharmacol. Sci.* **28**, 608–614.
- Cooper, J.A., Gould, K.L., Cartwright, C.A., and Hunter, T. (1986). Tyr527 is phosphorylated in pp60c-src: implications for regulation. *Science* **237**, 1431–1434.
- Cowan-Jacob, S.W., Fendrich, G., Manley, P.W., Jahnke, W., Fabbro, D., Liebetanz, J., and Meyer, T. (2005). The crystal structure of a c-Src complex in an active conformation suggests possible steps in c-Src activation. *Structure* **13**, 861–871.
- Crocker, J.C., and Grier, D.G. (1996). Methods of Digital Video Microscopy for Colloidal Studies. *J. Colloid Interface Sci.* **179**, 298–310.
- Dagliyan, O., Shirvanyants, D., Karginov, A.V., Ding, F., Fee, L., Chandrasekaran, S.N., Freisinger, C.M., Smolen, G.A., Huttenlocher, A., Hahn, K.M., and Dokholyan, N.V. (2013). Rational design of a ligand-controlled protein conformational switch. *Proc. Natl. Acad. Sci. USA* **110**, 6800–6804.
- Dagliyan, O., Tarnawski, M., Chu, P.-H., Shirvanyants, D., Schlichting, I., Dokholyan, N.V., and Hahn, K.M. (2016). Engineering extrinsic disorder to control protein activity in living cells. *Science* **354**, 1441–1444.
- de Mol, N.J., Dekker, F.J., Broutin, I., Fischer, M.J.E., and Liskamp, R.M.J. (2005). Surface plasmon resonance thermodynamic and kinetic analysis as a strategic tool in drug design. Distinct ways for phosphopeptides to plug into Src- and Grb2 SH2 domains. *J. Med. Chem.* **48**, 753–763.
- Edelstein, A.D., Tsuchida, M.A., Amodaj, N., Pinkard, H., Vale, R.D., and Stuurman, N. (2014). Advanced methods of microscope control using μ Manager software. *J. Biol. Methods* **1**, e10.
- Ewers, H., Smith, A.E., Sbalzarini, I.F., Lilie, H., Koumoutsakos, P., and Helenius, A. (2005). Single-particle tracking of murine polyoma virus-like particles on live cells and artificial membranes. *Proc. Natl. Acad. Sci. USA* **102**, 15110–15115.
- Ferrari, R., Manfroi, A.J., and Young, W.R. (2001). Strongly and weakly self-similar diffusion. *Physica D* **154**, 111–137.
- Fincham, V.J., Chudleigh, A., and Frame, M.C. (1999). Regulation of p190 Rho-GAP by v-Src is linked to cytoskeletal disruption during transformation. *J. Cell Sci.* **112**, 947–956.
- Flynn, J.M., Levchenko, I., Seidel, M., Wickner, S.H., Sauer, R.T., and Baker, T.A. (2001). Overlapping recognition determinants within the ssrA degradation tag allow modulation of proteolysis. *Proc. Natl. Acad. Sci. USA* **98**, 10584–10589.
- Fortin, F.-A., de Rainville, F.-M., Gardner, M.-A., Parizeau, M., and Gagné, C. (2012). DEAP: Evolutionary Algorithms Made Easy. *J. Mach. Learn. Res.* **13**, 2171–2175.
- Gardel, M.L., Schneider, I.C., Aratyn-Schaus, Y., and Waterman, C.M. (2010). Mechanical integration of actin and adhesion dynamics in cell migration. *Annu. Rev. Cell Dev. Biol.* **26**, 315–333.
- Gelman, A., and Rubin, D.B. (1992). Inference from Iterative Simulation Using Multiple Sequences. *Stat. Sci.* **7**, 457–472.
- Geweke, J. (1992). Evaluating the Accuracy of Sampling-Based Approaches to the Calculation of Posterior Moments. *BAYESIAN STATISTICS* **4**, 169–193.
- Githaka, J.M., Vega, A.R., Baird, M.A., Davidson, M.W., Jaqaman, K., and Touret, N. (2016). Ligand-induced growth and compaction of CD36 nanoclusters enriched in Fyn induces Fyn signaling. *J. Cell Sci.* **129**, 4175–4189.
- Griffié, J., Burn, G.L., Williamson, D.J., Peters, R., Rubin-Delanchy, P., and Owen, D.M. (2018). Dynamic Bayesian Cluster Analysis of Live-Cell Single Molecule Localization Microscopy Datasets. *Small Methods* **2**, 1800008.
- Grimm, J.B., English, B.P., Chen, J., Slaughter, J.P., Zhang, Z., Revyakin, A., Patel, R., Macklin, J.J., Normanno, D., Singer, R.H., et al. (2015). A general method to improve fluorophores for live-cell and single-molecule microscopy. *Nat. Methods* **12**, 244–250.
- Gulyani, A., Vitriol, E., Allen, R., Wu, J., Gremyachinskiy, D., Lewis, S., Dewar, B., Graves, L.M., Kay, B.K., Kuhlman, B., et al. (2011). A biosensor generated via high-throughput screening quantifies cell edge Src dynamics. *Nat. Chem. Biol.* **7**, 437–444.
- Guntas, G., Hallett, R.A., Zimmerman, S.P., Williams, T., Yumerefendi, H., Bear, J.E., and Kuhlman, B. (2015). Engineering an improved light-induced dimer (iLID) for controlling the localization and activity of signaling proteins. *Proc. Natl. Acad. Sci. USA* **112**, 112–117.
- Haario, H., Laine, M., Mira, A., and Saksman, E. (2006). DRAM: Efficient adaptive MCMC. *Stat. Comput.* **16**, 339–354.
- Han, S.J., Oak, Y., Groisman, A., and Danuser, G. (2015). Traction microscopy to identify force modulation in subresolution adhesions. *Nat. Methods* **12**, 653–656.

- Hersch, G.L., Baker, T.A., and Sauer, R.T. (2004). SspB delivery of substrates for ClpXP proteolysis probed by the design of improved degradation tags. *Proc. Natl. Acad. Sci. USA* *101*, 12136–12141.
- Hodgson, L., Shen, F., and Hahn, K. (2010). Biosensors for characterizing the dynamics of rho family GTPases in living cells. *Curr. Protoc. Cell Biol. Chapter 14*, Unit 14.11.1-26.
- Hodgson, L., Spiering, D., Sabouri-Ghomi, M., Dagliyan, O., DerMardirossian, C., Danuser, G., and Hahn, K.M. (2016). FRET binding antenna reports spatiotemporal dynamics of GDI-Cdc42 GTPase interactions. *Nat. Chem. Biol.* *12*, 802–809.
- Huveneers, S., and Danen, E.H.J. (2009). Adhesion signaling - crosstalk between integrins, Src and Rho. *J. Cell Sci.* *122*, 1059–1069.
- Jares-Erijman, E.A., and Jovin, T.M. (2003). FRET imaging. *Nat. Biotechnol.* *21*, 1387–1395.
- Karginov, A.V., Ding, F., Kota, P., Dokholyan, N.V., and Hahn, K.M. (2010). Engineered allosteric activation of kinases in living cells. *Nat. Biotechnol.* *28*, 743–747.
- Karginov, A.V., Tsygankov, D., Berginski, M., Chu, P.-H., Trudeau, E.D., Yi, J.J., Gomez, S., Elston, T.C., and Hahn, K.M. (2014). Dissecting motility signaling through activation of specific Src-effector complexes. *Nat. Chem. Biol.* *10*, 286–290.
- Keppler, A., Gendreizig, S., Gronemeyer, T., Pick, H., Vogel, H., and Johnsson, K. (2003). A general method for the covalent labeling of fusion proteins with small molecules in vivo. *Nat. Biotechnol.* *21*, 86–89.
- Kmiecik, T.E., and Shalloway, D. (1987). Activation and suppression of pp60c-src transforming ability by mutation of its primary sites of tyrosine phosphorylation. *Cell* *49*, 65–73.
- König, I., Zarrine-Afsar, A., Aznauryan, M., Soranno, A., Wunderlich, B., Dingfelder, F., Stüber, J.C., Plückthun, A., Nettels, D., and Schuler, B. (2015). Single-molecule spectroscopy of protein conformational dynamics in live eukaryotic cells. *Nat. Methods* *12*, 773–779.
- Koudelková, L., Pataki, A.C., Tolde, O., Pavlik, V., Nobis, M., Gemperle, J., Anderson, K., Brábek, J., and Rosel, D. (2019). Novel FRET-Based Src Biosensor Reveals Mechanisms of Src Activation and Its Dynamics in Focal Adhesions. *Cell Chem. Biol.* *26*, 255–268.e4.
- Kusumi, A., Ike, H., Nakada, C., Murase, K., and Fujiwara, T. (2005). Single-molecule tracking of membrane molecules: plasma membrane compartmentalization and dynamic assembly of raft-philic signaling molecules. *Semin. Immunol.* *17*, 3–21.
- Kypta, R.M., Goldberg, Y., Ulug, E.T., and Courtneidge, S.A. (1990). Association between the PDGF receptor and members of the src family of tyrosine kinases. *Cell* *62*, 481–492.
- Ladbury, J.E., and Arold, S.T. (2011). Energetics of Src homology domain interactions in receptor tyrosine kinase-mediated signaling. *Methods Enzymol.* *488*, 147–183.
- Laura, R.P., Witt, A.S., Held, H.A., Gerstner, R., Deshayes, K., Koehler, M.F.T., Kosik, K.S., Sidhu, S.S., and Lasky, L.A. (2002). The Erbin PDZ domain binds with high affinity and specificity to the carboxyl termini of delta-catenin and ARVCF. *J. Biol. Chem.* *277*, 12906–12914.
- Le Roux, A.-L., Busquets, M.A., Sagués, F., and Pons, M. (2016). Kinetics characterization of c-Src binding to lipid membranes: Switching from labile to persistent binding. *Colloids Surf. B Biointerfaces* *138*, 17–25.
- Lee, J., Natarajan, M., Nashine, V.C., Socolich, M., Vo, T., Russ, W.P., Benkovic, S.J., and Ranganathan, R. (2008). Surface sites for engineering allosteric control in proteins. *Science* *322*, 438–442.
- Letts, V.A., Felix, R., Biddlecome, G.H., Arikath, J., Mahaffey, C.L., Valenzuela, A., Bartlett, F.S., 2nd, Mori, Y., Campbell, K.P., and Frankel, W.N. (1998). The mouse stargazer gene encodes a neuronal Ca²⁺-channel gamma subunit. *Nat. Genet.* *19*, 340–347.
- Levchenko, I., Seidel, M., Sauer, R.T., and Baker, T.A. (2000). A specificity-enhancing factor for the ClpXP degradation machine. *Science* *289*, 2354–2356.
- Levet, F., Hosity, E., Kechkar, A., Butler, C., Beghin, A., Choquet, D., and Sibarita, J.-B. (2015). SR-Tesseler: a method to segment and quantify localization-based super-resolution microscopy data. *Nat. Methods* *12*, 1065–1071.
- Li, J., Rix, U., Fang, B., Bai, Y., Edwards, A., Colinge, J., Bennett, K.L., Gao, J., Song, L., Eschrich, S., et al. (2010). A chemical and phosphoproteomic characterization of dasatinib action in lung cancer. *Nat. Chem. Biol.* *6*, 291–299.
- Lietha, D., Cai, X., Ceccarelli, D.F.J., Li, Y., Schaller, M.D., and Eck, M.J. (2007). Structural basis for the autoinhibition of focal adhesion kinase. *Cell* *129*, 1177–1187.
- Los, G.V., Encell, L.P., McDougall, M.G., Hartzell, D.D., Karassina, N., Zimprich, C., Wood, M.G., Learish, R., Ohana, R.F., Urh, M., et al. (2008). HaloTag: a novel protein labeling technology for cell imaging and protein analysis. *ACS Chem. Biol.* *3*, 373–382.
- Lu, S., Seong, J., Wang, Y., Chang, S.C., Eichorst, J.P., Ouyang, M., Li, J.Y.-S., Chien, S., and Wang, Y. (2014). Decipher the dynamic coordination between enzymatic activity and structural modulation at focal adhesions in living cells. *Sci. Rep.* *4*, 5756.
- Lungu, O.I., Hallett, R.A., Choi, E.J., Aiken, M.J., Hahn, K.M., and Kuhlman, B. (2012). Designing photoswitchable peptides using the AsLOV2 domain. *Chem. Biol.* *19*, 507–517.
- Machacek, M., Hodgson, L., Welch, C., Elliott, H., Pertz, O., Nalbant, P., Abell, A., Johnson, G.L., Hahn, K.M., and Danuser, G. (2009). Coordination of Rho GTPase activities during cell protrusion. *Nature* *461*, 99–103.
- Machiyama, H., Yamaguchi, T., Sawada, Y., Watanabe, T.M., and Fujita, H. (2015). SH3 domain of c-Src governs its dynamics at focal adhesions and the cell membrane. *FEBS J.* *282*, 4034–4055.
- Marston, D.J., Vilela, M., Huh, J., Ren, J., Azoitei, M.L., Glekas, G., Danuser, G., Sondek, J., and Hahn, K.M. (2020). Multiplexed GTPase and GEF biosensor imaging enables network connectivity analysis. *Nat. Chem. Biol.* *16*, 826–833.
- Milano, V., Piao, Y., LaFortune, T., and de Groot, J. (2009). Dasatinib-induced autophagy is enhanced in combination with temozolomide in glioma. *Mol. Cancer Ther.* *8*, 394–406.
- Miles, P. (2019). pymcmcstat: A Python Package for Bayesian Inference Using Delayed Rejection Adaptive Metropolis. *J. Open Source Softw.* *4*, 1417.
- Mkaddem, S.B., Murua, A., Flament, H., Titeca-Beauport, D., Bounaix, C., Danelli, L., Launay, P., Benhamou, M., Blank, U., Daugas, E., et al. (2017). Lyn and Fyn function as molecular switches that control immunoreceptors to direct homeostasis or inflammation. *Nat. Commun.* *8*, 246.
- Mo, G.C.H., Ross, B., Hertel, F., Manna, P., Yang, X., Greenwald, E., Booth, C., Plummer, A.M., Tenner, B., Chen, Z., et al. (2017). Genetically encoded biosensors for visualizing live-cell biochemical activity at super-resolution. *Nat. Methods* *14*, 427–434.
- Murakoshi, H., Iino, R., Kobayashi, T., Fujiwara, T., Ohshima, C., Yoshimura, A., and Kusumi, A. (2004). Single-molecule imaging analysis of Ras activation in living cells. *Proc. Natl. Acad. Sci. USA* *101*, 7317–7322.
- Nalbant, P., Hodgson, L., Kraynov, V., Toutchkine, A., and Hahn, K.M. (2004). Activation of endogenous Cdc42 visualized in living cells. *Science* *305*, 1615–1619.
- Nasertorabi, F., Tars, K., Becherer, K., Kodandapani, R., Liljas, L., Vuori, K., and Ely, K.R. (2006). Molecular basis for regulation of Src by the docking protein p130Cas. *J. Mol. Recognit.* *19*, 30–38.
- Niopek, D., Benzinger, D., Roensch, J., Draebing, T., Wehler, P., Eils, R., and Di Ventura, B. (2014). Engineering light-inducible nuclear localization signals for precise spatiotemporal control of protein dynamics in living cells. *Nat. Commun.* *5*, 4404.
- Ogawa, A., Takayama, Y., Sakai, H., Chong, K.T., Takeuchi, S., Nakagawa, A., Nada, S., Okada, M., and Tsukihara, T. (2002). Structure of the carboxyl-terminal Src kinase, Csk. *J. Biol. Chem.* *277*, 14351–14354.
- Oliveo-Marin, J.-C. (2002). Extraction of spots in biological images using multiscale products. *Pattern Recognit.* *35*, 1989–1996.
- Ostermeier, M. (2009). Designing switchable enzymes. *Curr. Opin. Struct. Biol.* *19*, 442–448.

- Owen, D.M., Rentero, C., Rossy, J., Magenau, A., Williamson, D., Rodriguez, M., and Gaus, K. (2010). PALM imaging and cluster analysis of protein heterogeneity at the cell surface. *J. Biophotonics* **3**, 446–454.
- Palacios, E.H., and Weiss, A. (2004). Function of the Src-family kinases, Lck and Fyn, in T-cell development and activation. *Oncogene* **23**, 7990–8000.
- Parsons, J.T., and Parsons, S.J. (1997). Src family protein tyrosine kinases: cooperating with growth factor and adhesion signaling pathways. *Curr. Opin. Cell Biol.* **9**, 187–192.
- Parsons, S.J., and Parsons, J.T. (2004). Src family kinases, key regulators of signal transduction. *Oncogene* **23**, 7906–7909.
- Payne, G., Shoelson, S.E., Gish, G.D., Pawson, T., and Walsh, C.T. (1993). Kinetics of p56lck and p60src Src homology 2 domain binding to tyrosine-phosphorylated peptides determined by a competition assay or surface plasmon resonance. *Proc. Natl. Acad. Sci. USA* **90**, 4902–4906.
- Persson, F., Lindén, M., Unoson, C., and Elf, J. (2013). Extracting intracellular diffusive states and transition rates from single-molecule tracking data. *Nat. Methods* **10**, 265–269.
- Pertz, O., Hodgson, L., Klemke, R.L., and Hahn, K.M. (2006). Spatiotemporal dynamics of RhoA activity in migrating cells. *Nature* **440**, 1069–1072.
- Pichot, C.S., Hartig, S.M., Xia, L., Arvanitis, C., Monisvais, D., Lee, F.Y., Frost, J.A., and Corey, S.J. (2009). Dasatinib synergizes with doxorubicin to block growth, migration, and invasion of breast cancer cells. *Br. J. Cancer* **101**, 38–47.
- Playford, M.P., and Schaller, M.D. (2004). The interplay between Src and integrins in normal and tumor biology. *Oncogene* **23**, 7928–7946.
- Qian, H., and Elson, E.L. (2002). Single-molecule enzymology: stochastic Michaelis-Menten kinetics. *Biophys. Chem.* **101–102**, 565–576.
- Rix, U., Hantschel, O., Dürmberger, G., Rensing Rix, L.L., Planyavsky, M., Fernbach, N.V., Kaube, I., Bennett, K.L., Valent, P., Colinge, J., et al. (2007). Chemical proteomic profiles of the BCR-ABL inhibitors imatinib, nilotinib, and dasatinib reveal novel kinase and nonkinase targets. *Blood* **110**, 4055–4063.
- Roskoski, R., Jr. (2004). Src protein-tyrosine kinase structure and regulation. *Biochem. Biophys. Res. Commun.* **324**, 1155–1164.
- Roskoski, R., Jr. (2015). Src protein-tyrosine kinase structure, mechanism, and small molecule inhibitors. *Pharmacol. Res.* **94**, 9–25.
- Rossy, J., Owen, D.M., Williamson, D.J., Yang, Z., and Gaus, K. (2013). Conformational states of the kinase Lck regulate clustering in early T cell signaling. *Nat. Immunol.* **14**, 82–89.
- Sakon, J.J., and Weninger, K.R. (2010). Detecting the conformation of individual proteins in live cells. *Nat. Methods* **7**, 203–205.
- Sandilands, E., Cans, C., Fincham, V.J., Brunton, V.G., Mellor, H., Prendergast, G.C., Norman, J.C., Superti-Furga, G., and Frame, M.C. (2004). RhoB and actin polymerization coordinate Src activation with endosome-mediated delivery to the membrane. *Dev. Cell* **7**, 855–869.
- Sandilands, E., Brunton, V.G., and Frame, M.C. (2007). The membrane targeting and spatial activation of Src, Yes and Fyn is influenced by palmitoylation and distinct RhoB/RhoD endosome requirements. *J. Cell Sci.* **120**, 2555–2564.
- Sato, I., Obata, Y., Kasahara, K., Nakayama, Y., Fukumoto, Y., Yamasaki, T., Yokoyama, K.K., Saito, T., and Yamaguchi, N. (2009). Differential trafficking of Src, Lyn, Yes and Fyn is specified by the state of palmitoylation in the SH4 domain. *J. Cell Sci.* **122**, 965–975.
- Saxton, M.J. (1997). Single-particle tracking: the distribution of diffusion coefficients. *Biophys. J.* **72**, 1744–1753.
- Schild, H.O. (1947). pA, a new scale for the measurement of drug antagonism. *Br. J. Pharmacol. Chemother.* **2**, 189–206.
- Sengupta, P., Jovanovic-Taliman, T., Skoko, D., Renz, M., Veatch, S.L., and Lippincott-Schwartz, J. (2011). Probing protein heterogeneity in the plasma membrane using PALM and pair correlation analysis. *Nat. Methods* **8**, 969–975.
- Shcherbakova, D.M., Sengupta, P., Lippincott-Schwartz, J., and Verkhusha, V.V. (2014). Photocontrollable fluorescent proteins for superresolution imaging. *Annu. Rev. Biophys.* **43**, 303–329.
- Shvartsman, D.E., Donaldson, J.C., Diaz, B., Gutman, O., Martin, G.S., and Henis, Y.I. (2007). Src kinase activity and SH2 domain regulate the dynamics of Src association with lipid and protein targets. *J. Cell Biol.* **178**, 675–686.
- Slattery, S.D., and Hahn, K.M. (2014). A High-Content Assay for Biosensor Validation and for Examining Stimuli that Affect Biosensor Activity. *Curr. Protoc. Cell Biol.* **65**, 14.15.1–31.
- Smith, A.W., Huang, H.H., Endres, N.F., Rhodes, C., and Groves, J.T. (2016). Dynamic organization of myristoylated src in the live cell plasma membrane. *J. Phys. Chem. B* **120**, 867–876.
- Song, H.K., and Eck, M.J. (2003). Structural basis of degradation signal recognition by SspB, a specificity-enhancing factor for the ClpXP proteolytic machine. *Mol. Cell* **12**, 75–86.
- Summy, J.M., and Gallick, G.E. (2003). Src family kinases in tumor progression and metastasis. *Cancer Metastasis Rev.* **22**, 337–358.
- Takeshita, K., Tezuka, T., Isozaki, Y., Yamashita, E., Suzuki, M., Kim, M., Yamanashi, Y., Yamamoto, T., and Nakagawa, A. (2012). Structural flexibility regulates phosphopeptide-binding activity of the tyrosine kinase binding domain of Cbl-c. *J. Biochem.* **152**, 487–495.
- Thomas, S.M., and Brugge, J.S. (1997). Cellular functions regulated by Src family kinases. *Annu. Rev. Cell Dev. Biol.* **13**, 513–609.
- Tsang, E., Giannetti, A.M., Shaw, D., Dinh, M., Tse, J.K.Y., Gandhi, S., Ho, H., Wang, S., Papp, E., and Bradshaw, J.M. (2008). Molecular mechanism of the Syk activation switch. *J. Biol. Chem.* **283**, 32650–32659.
- Vinkenborg, J.L., Evers, T.H., Reulen, S.W.A., Meijer, E.W., and Merkx, M. (2007). Enhanced sensitivity of FRET-based protease sensors by redesign of the GFP dimerization interface. *ChemBioChem* **8**, 1119–1121.
- Wah, D.A., Levchenko, I., Baker, T.A., and Sauer, R.T. (2002). Characterization of a specificity factor for an AAA+ ATPase: assembly of SspB dimers with ssrA-tagged proteins and the ClpX hexamer. *Chem. Biol.* **9**, 1237–1245.
- Waskom, M. (2021). seaborn: statistical data visualization. *J. Open Source Softw.* **6**, 3021.
- Webb, D.J., Donais, K., Whitmore, L.A., Thomas, S.M., Turner, C.E., Parsons, J.T., and Horwitz, A.F. (2004). FAK-Src signalling through paxillin, ERK and MLCK regulates adhesion disassembly. *Nat. Cell Biol.* **6**, 154–161.
- Yeatman, T.J. (2004). A renaissance for SRC. *Nat. Rev. Cancer* **4**, 470–480.
- Zawistowski, J.S., Sabouri-Ghomi, M., Danuser, G., Hahn, K.M., and Hodgson, L. (2013). A RhoC biosensor reveals differences in the activation kinetics of RhoA and RhoC in migrating cells. *PLoS ONE* **8**, e79877.

STAR★METHODS

KEY RESOURCES TABLE

REAGENT or RESOURCE	SOURCE	IDENTIFIER
Antibodies		
FLAG	Sigma-Aldrich	F7425-.2MG; RRID:AB_439687
Myc-Tag (71D10) Rabbit mAb	Cell Signaling Technology	2278S; RRID:AB_490778
Src (32G6) Rabbit mAb	Cell Signaling Technology	2123T; RRID:AB_1102399
Phospho-Src Family (Tyr416) (D49G4) Rabbit mAb	Cell Signaling Technology	6943T; RRID:AB_10013641
Phospho-Src (Tyr527) Antibody	Cell Signaling Technology	2105T; RRID:AB_331034
B-Actin (8H10D10) Mouse mAb	Cell Signaling Technology	3700S; RRID:AB_11188565
Paxillin	Santa Cruz Technology	sc-365379; RRID:AB_10859206
FAK	Cell Signaling Technology	3285T; RRID:AB_2269034
Vinculin	Sigma-Aldrich	V9131-100UL; RRID:AB_477629
Anti-Phosphotyrosine	ECM Biosciences	PM3751; RID:AB_1944435
Chemicals, peptides, and recombinant proteins		
Dasatinib	MedChem Express	HY-10181
PDGF	R&D system	220-BB
Dulbecco's Modified Eagle's Medium	Cellgro	15-013-CV
Fetal Bovine Serum	Hyclone	SH30088.03
GlutaMax	GIBCO	35050061
Hams/F12	Caisson Labs	HFL12
HEPES	GIBCO	15630106
DPBS	Corning	MT21031CV
IP lysis buffer	Pierce	87788
Protease inhibitors	Millipore Sigma	11873580001
Phosphatase inhibitors, PhosSTOP	Roche	4906845001
2-mercaptoethanol	Biorad	1610710
4x Laemmli Sample Buffer	Bio-Rad	1610747
Fugene6	Promega	E2691
Lipofectamine and Plus reagent	Invitrogen	A12621
Deposited data		
Structure of SspB-ssrA complex	Song and Eck, 2003	PDB:1OX9
Structure of unphosphorylated c-Src	Cowan-Jacob et al., 2005	PDB: 1Y57
Structure of CSK	Ogawa et al., 2002	PDB: 1K9A
Structure of tyrosine kinase binding domain of Cbl-c	Takeshita et al., 2012	PDB: 3VRO
Structure of PTPN-22	RCSB PDB	PDB: 3BRH
Structure of p130cas	Nasertorabi et al., 2006	PDB: 1X27
Experimental models: Cell lines		
Mouse embryo fibroblast, Tet-Off	ClonTech	630914
COS7	ATCC	CRL-1651; RRID:CVCL_0224
HEK293T	ATCC	CRL-11268; RRID:CVCL_1926
Software and algorithms		
GraphPad Prism version 8.4.3	GraphPad Software	https://www.graphpad.com/ ; RRID:SCR_002798
MATLAB 2018, 2019	The MathWorks, Inc.	https://www.mathworks.com/ ; RRID:SCR_001622
Seaborn, version 0.10.1	Waskom, 2021	https://seaborn.pydata.org/ ; RRID:SCR_018132
Metamorph	Molecular Devices, LLC.	https://www.moleculardevices.com/ ; RRID:SCR_002368
Micromanager 2.0 gamma	Edelstein et al., 2014	https://micro-manager.org/ ; RRID:SCR_016865
Cluster detection and analysis; kinetic modeling	This paper	https://zenodo.org/record/5508399

RESOURCE AVAILABILITY

Lead contact

Further information and requests for resources and reagents should be directed to and will be fulfilled by the Lead Contact, Klaus M. Hahn (khahn@med.unc.edu).

Materials availability

Plasmids generated in this study will be deposited to Addgene and are available from the Lead Contact with a completed Materials Transfer Agreement.

Stable cell lines generated in this study will be available upon request from the lead contact.

Data and code availability

- Original western blot images and microscopy data reported in this paper will be shared by the lead contact upon request.
- The code supporting the current study has been publicly released on GitHub and archived with Zenodo. DOIs are listed in the [Key Resources Table](#).
- Any additional information required to reanalyze the data reported in this paper is available from the lead contact upon request.

EXPERIMENTAL MODEL AND SUBJECT DETAILS

HEK293T and COS-7 cells were obtained from the ATCC (<https://www.atcc.org/>). Authentication was performed by the companies. MEFs were purchased from Clontech, who state that they were derived from NIH 3T3 cells (RRID:CVCL_0594) authenticated by STR. The ATCC states that the COS-7 cells were authenticated by morphology and were derived from ATCC CCL-70, which were authenticated by Karyotype. HEK293T cells were authenticated by STR.

Cells (MEF, HeLa and HEK293T) were maintained in Dulbecco's Modified Eagle's Medium (DMEM) (Cellgro, 15-013-CV) supplemented with 10% fetal bovine serum (FBS) (Hyclone, SH30088.03) and 1X GlutaMax (GIBCO, 35050061). For single cell imaging, cells were re-plated on fibronectin-coated coverslips and allowed to attach for at least 2 hours. Before imaging, the media was replaced with Hams/F12 (Caisson Labs, HFL12) supplemented with 5% FBS and 10 mM HEPES (GIBCO, 15630106).

METHOD DETAILS

Epifluorescence microscopy

Epifluorescence imaging was performed on an Olympus IX-81 microscope equipped with a UPlanFLN 40x objective (Pil, N.A 1.30). Metamorph software (Molecular Devices) was used to control the microscope and acquire images. The light source was a 100 Watt mercury arc lamp. All dichroic beamsplitters and bandpass filters were purchased from Semrock unless otherwise indicated. For assessing the localization of Src and SspB in LinXE and HeLa cells, a FF444/521/608 dichroic beamsplitter and either Chroma HQ470/40X (GFP) or Zeiss BP-585/35 (mCherry) bandpass filter were used to select excitation wavelengths. Emission selection was accomplished with either a Chroma HQ525/50 m (GFP) or FF-647/57 (mCherry) filter. Images were collected with a Photometrics Cool Snap ES2 CCD camera. For FRET imaging in MEF cells, a FF462/523 dichroic beamsplitter and either a FF-434/17 (CFP) or FF-510/10 (YFP) bandpass filter were used to select excitation wavelengths. Simultaneous collection of CFP and YFP emission was accomplished with an Andor TuCam two camera adaptor using a FF509-FDi01 dichroic beamsplitter, as well as FF-550/49 and FF-482/35 bandpass filters. Images were collected with two Hamamatsu Flash 4 V2 sCMOS cameras. The two cameras were manually aligned prior to image analysis and images were further aligned after collection using a custom MATLAB (MathWorks) script described previously ([Hodgson et al., 2010](#)). Image processing, including flat-field correction, background subtraction, bleed-through subtraction, photobleaching calculations, and ratio calculations were accomplished using a custom MATLAB script ([Hodgson et al., 2010](#)).

In-cell kinase activity assay

HEK293T cells were seeded into 6-well plates with 0.8 M cells per well. The next day cells were transfected with the indicated constructs using Fugene6 (Promega) according to the manufacturer's protocol. At 24 h post-transfection cells were collected by removing media and washing 1X with 1 mL ice-cold DPBS. To each well, 250 μ L of IP lysis buffer (Pierce) was added and cells were removed with a cell lifter (Corning), followed by pipetting the entire volume over the surface of the well several times to remove remaining cells and mix the lysate. Lysis buffer contained protease inhibitors (cOmplete EDTA-free; Millipore Sigma) and phosphatase inhibitors (PhosSTOP; Roche). Lysate was then transferred to pre-chilled Eppendorf tubes on ice and placed on rotating mixer for 20 m at 4C. Following incubation lysates were centrifuged at 6000 *rcf.* for 10 m at 4C. Supernatant was removed and combined with 4X Laemmli sample buffer (10% 2-mercaptoethanol) and boiled for 5 m. Samples were western blotted for total phosphotyrosine and kinase expression. Initial optimization of transfection conditions was required to identify a kinase expression level that produced detectable changes in total cell phosphotyrosine between controls.

Co-immunoprecipitation assay

HEK293T cells were transfected and lysed as described for the in-cell kinase activity assay. Following centrifugation of lysates, 20 μ L were removed from each sample to assess lysate protein expression. Two μ L Anti Flag M2 (1 mg/mL) were added to each sample of the remaining lysate. They were then placed on a rotating mixer at 4 C for 3 h. Following incubation, 30 μ L of PureProteome Protein G magnetic beads (Millipore Sigma) were added to each sample, which were then incubated on a rotating mixer at room temperature for 15 m. Following incubation, samples were washed 3X with IP lysis buffer and resuspended in sample buffer, boiled for 5 m, and stored at 4 C. Samples were western blotted for indicated proteins. Kinase-dead mutants (D388R) tagSrc and tagFyn were used for co-immunoprecipitation assay for even expression levels (Figures 2C, S1A, and S1F).

Identification of effector binding sites

Analysis of Src effector binding sites was accomplished by searching the Research Collaboratory for Structural Bioinformatics Protein Data Bank (RCSB PDB) for X-ray crystal structures of Src bound to other proteins. We identified the following structures: active Src (1Y57), Csk (1K9A), Cbl-c (3VRO), PTPN-22 (3BRH), and p130cas (1X27). The structures were loaded in PyMOL (The PyMOL Molecular Graphics System, Version 2.1.0 Schrodinger, LLC) and aligned using Src as a common reference.

Cell rounding

HEK293T cells were plated on fibronectin-coated coverslips and allowed to spread overnight. The next day, cells were transfected with the indicated constructs using Fugene6 (Promega) according to the manufacturer's protocol. At 24 h post-transfection cells were imaged in Ham's F-12 medium (Kaighn's Modification) (Caisson Laboratories, Inc) supplemented with 1 mM HEPES and 5% FBS. Images were acquired using differential interference contrast (DIC) microscopy. Image fields were scored for the number of rounded cells by an evaluator unaware of the source of each sample.

Modeling of binding curves

We used the law of mass action to model the binding equilibrium of Src and SspB. We describe the reversible binding of SspB to Src in terms of their equilibrium dissociation constant, K_D .

$$K_D = \frac{k_{off}}{k_{on}} = \frac{[SspB_{free}][Src_{free}]}{[Complex]}$$

Substitution of the equation to describe K_D solely in terms of total concentrations of SspB, Src, and the SspB-Src complex gives:

$$K_D = \frac{([SspB_{total}] - [Complex])([Src_{total}] - [Complex])}{[Complex]}$$

Rearrangement of the equation and application of the quadratic formula yields:

$$[PA] = \frac{([SspB_{total}] + [Src_{total}] + [K_D]) \pm \sqrt{([SspB_{total}] + [Src_{total}] + [K_D])^2 - 4[SspB_{total}][Src_{total}]}}{2}$$

Where,

$$\% \text{ Src Bound} = \frac{[PA]}{[Src_{total}]} * 100$$

We input the final formula into MATLAB to plot binding curves for a range of SspB concentrations given the concentration of Src and the affinity of their interaction.

High-content assay

High-content live cell FRET imaging was performed as described previously (Slattery and Hahn, 2014). Briefly, HEK293T cells were seeded onto 96-well plates and cells were transfected with the indicated constructs, using Lipofectamine and Plus reagent (Invitrogen) according to the manufacturer's protocol. Plates were imaged with an automated microscope (Olympus IX-81 with automated stage, filter wheels and X/Y/Z stage with autofocus) and Metamorph software was used to image each well for CFP, YFP, and FRET emission. A custom-written MATLAB script was used to calculate the sum intensity of each well and perform background subtraction, bleed-through corrections, and normalization of FRET/Donor ratios for each well.

Fluorometer assay

Fluorometer assays were performed as described previously (Pertz et al., 2006). Briefly, HEK293T cells were seeded into 6-well plates and transfected with the indicated constructs, using Lipofectamine and Plus reagent (Invitrogen) according to the manufacturer's protocol. At 24 h post transfection cells were harvested by trypsinization, then resuspended in DPBS (10% FBS). The cells were centrifuged at 1000 *rcf.*, supernatant was removed, they were resuspended in 700 μ L DPBS (10% FBS), and placed in

Eppendorf tubes on ice, protected from light. To collect CFP and FRET emission, samples were excited at 433 nm and emission was collected from 450 to 600 nm. To collect YFP emission, samples were excited at 505 nm and emission was measured at 525 nm. Cells transfected with empty cDNA (pBABE-puro) was used to measure autofluorescence and light scatter, which was subtracted from the data. FRET emission was corrected for bleed-through and FRET/Donor ratio was calculated by dividing corrected FRET emission at 525 nm by CFP emission at 474 nm.

Immunofluorescence

For measurement of endogenous Src expression level and variability, MEF cells were processed as follows: Cells were fixed with 3.7% paraformaldehyde for 20 min at room temperature and washed 3X with DPBS, then permeabilized with Triton X-100 0.1% solution in DPBS for 5 min and washed 3X with DPBS. The cells were next blocked with 1% BSA and 1% FBS in DPBS for 1 h at room temperature, then stained with primary and secondary antibodies at indicated dilutions in blocking buffer for 1 hour and washed 3X with DPBS after each incubation.

PDGF treatment

For assessment of the FRET biosensor's response to PDGF treatment (Figure S2J), LINXE cells were seeded in 12 well plates for at least four hours and transfected with the binder/tag FRET biosensor or control plasmids (tagSrc-mCerulean with yPet) using Fugene6 (Promega) according to the manufacturer's protocol. After overnight incubation, cells were transferred to glass bottom dishes (MatTek, P35GC-1.5-14-C) coated with poly-D-lysine. Imaging was performed on an Olympus IX-81 microscope equipped with an UPlanFLN 10X objective (N.A 0.3). For excitation, we used Chroma ET436/20 (CFP) and ET500/20 (YFP) bandpass filters combined with Chroma dichroic ET445/505/580. To collect emission we used ET470/24 (Chroma) for CFP and ET535/30 (Chroma) for YFP (or FRET). Images were collected with a Hamamatsu Flash 4 sCMOS camera. PDGF (50 ng/ml) was added at 5 minutes after beginning acquisition.

Single molecule microscopy

Single molecule tracking was performed on a home-built TIRF microscope based on an IX81 microscope body (Olympus) and equipped with four solid-state lasers (Coherent OBIS 405 nm, 488 nm, 561 nm and 647 nm). A four-band dichroic mirror (DM: Di01-R405/488/561/635, Semrock) was used for multi-color imaging. Fluorescence images were collected using a 150 X TIRF objective (UAPON 150XOTIRF, NA 1.45, Olympus), and projected to an electron-multiplying charge-coupled device (EMCCD) camera (Evolve® 512 Delta, Photometrics). A 10-position emission filter wheel (Sutter Instruments) and imaging splitting optics (W-View GEMINI, Hamamatsu) were mounted in front of the camera to flexibly switch between different imaging modes. For dual-color SPT, the filter settings were as follows: in GEMINI, DM (T647lpxr, Chroma), Long-pass filter (FF01-698/70, Semrock) and short-pass filter (FF01-600/52, Semrock); the emission filter wheel was set to empty. For correlative adhesion and dual-color SPT: in the GEMINI, the short-pass filter was removed; the emission filter wheel was set to HQ525/50 M (Chroma) for EGFP-labeled adhesion marker imaging, and was switched to ET570lp (Chroma) for dual-color SPT. The system was controlled by the open-source software Micromanager (Edelstein et al., 2014).

Single molecule tracking

Single B/T MEF cells were imaged for 60 s at 50 Hz, generating 3000 frame videos. We first applied à trous-wavelet decomposition (Olivo-Marin, 2002) to extract individual single molecules. Each identified molecule was then fit with a 2D Gaussian function to obtain a precise centroid. We then adopted a well-established trajectory-linking algorithm to identify the same single molecule in successive frames (Crocker and Grier, 1996).

Single molecule diffusional analysis

The MSD at different time lags $\tau = n\Delta t$ was calculated as follows:

$$MSD(\tau) = \langle (x_{\tau+k} - x_{\tau})^2 + (y_{\tau+k} - y_{\tau})^2 \rangle,$$

where x_{i+k} and y_{i+k} describe a position following a time interval k after starting at x_{τ} and y_{τ} . To determine the diffusion coefficient of each track, the MSD curves were fitted to a nonlinear anomalous diffusion model:

$$MSD(\tau) = 4D\tau^{\alpha} + 4\sigma^2,$$

where D is the diffusion coefficient, α is the anomalous exponent, and σ is the localization precision. To obtain a reliable estimation of the diffusion coefficient, the minimum track length was set to 12 frames (Qian and Elson, 2002; Saxton, 1997).

We used moment scaling spectrum (MSS) analysis to categorize trajectories into diffusive modes, such as pure Brownian, confined (sub-diffusive) or directional (super-diffusive) movement (Ferrari et al., 2001). The moments of displacement of order ν is defined as:

$$MSS(\tau, \nu) = \langle (x_{\tau+k} - x_{\tau})^{\nu} + (y_{\tau+k} - y_{\tau})^{\nu} \rangle,$$

where τ is the time lag. The MSD is a special case where $\nu = 2$. These moments were calculated for $\nu = 0\sim 6$.

We also used a Hidden Markov model (HMM) approach to annotate the instantaneous diffusive behavior of trajectories using a previously described method (Persson et al., 2013). Trajectories with at least 5 frames were analyzed by variational Bayes single particle tracking, producing per-frame classification into discrete diffusive states based on a Brownian motion approximation. After examination of 1, 2, 3, 4, and 5-state diffusional models, two diffusive states were sufficient to explain the dataset based on an elbow analysis of the model scores. Each cell was analyzed as a separate dataset, and variability in the HMM parameters was reported over cells. The number of iterations was set to 25, bootstrapping to 100, diffusional prior to $[0.0001, 5] \mu\text{m}^2/\text{s}$, and dwell time prior to $[40, 400]$ ms. Occasionally frames were missing within trajectories, so prior to HMM analysis, these frames were interpolated by minimizing the sum of squares of the second derivative at the gap (see Source Code). After construction of the HMM, the interpolated frames were removed.

Quantification of adhesion morphology

BT MEF cells were transfected with paxillin-EGFP or control constructs (Figure S5) and stained with different adhesion protein antibodies (Paxillin: Santa Cruz Technology, sc-365379; FAK: Cell Signaling Technology, 3285T; Vinculin: Sigma-Aldrich, V9131-100UL). Adhesion images were taken on the home-built TIRF microscope described above, and adhesion morphology was characterized by a well-established adhesion-processing pipeline (Berginski et al., 2011) with a few modifications. Briefly, raw images were first filtered with a morphological top-hat operator and binarized with a wavelet decomposition approach (Olivo-Marin, 2002). A watershed algorithm was then applied to separate close, contacting adhesions. Quantitation of adhesion morphology (e.g., areas, eccentricity) was accomplished using the *regionprops* function of MATLAB. The full implementation of this can be found in the Source Code.

Quantification of FAK (or tagFAK) and binder intensity on adhesions

Paxillin-EGFP was used to identify adhesions using the approach described above. The adhesion mask was then mapped to the FAK-mCherry (or tagFAK-mCherry) channel. The average FAK intensity was extracted using the *regionprops* function of MATLAB and corrected by subtracting the overall cytosolic FAK intensity. The average binder intensity per adhesion was obtained similarly, except that the background was calculated locally by taking the mean intensity of a 3-pixel band surrounding each adhesion. The percentage binder intensity increase over background was shown. The full implementation of this can be found in the Source Code.

Normalized track density and track recruitment within adhesions

Tracks were considered 'on adhesion' if their centroid was within the adhesion. For each cell, absolute track centroid densities (also 'track densities') were calculated by counting the number of 'on adhesion' tracks and dividing by the area of the adhesions. Absolute track densities were normalized to the average track density within all adhesions, resulting in a dimensionless quantity labeled 'relative track density' in Figure 5D. Similarly, tracks were considered recruited to adhesions from the cytoplasm if the first frame of the track was inside an adhesion. Absolute cytoplasmic recruitment densities were calculated by counting the number of events and dividing by the area of the adhesions. The relative cytoplasmic recruitment density was similarly normalized to the average cytoplasmic recruitment density within all adhesions, resulting in the dimensionless quantity 'relative cyto. recruitment density' in Figure 5D. Absolute membrane recruitment influx was calculated by counting the number of tracks that diffused into adhesions from outside, then dividing by the perimeter of the adhesions. The relative membrane recruitment influx was normalized to the average membrane recruitment influx in all adhesions, resulting in the dimensionless quantity 'relative memb. recruitment influx' in Figure 5D. The adhesion size categories chosen reflect previously described bins for nascent adhesions ($0.05\text{--}0.25 \mu\text{m}^2$), focal complexes ($0.25\text{--}1 \mu\text{m}^2$), and focal adhesions ($1\text{--}5 \mu\text{m}^2$) (Gardel et al., 2010).

Drug treatment

BT MEFs were cultured in 100 pg doxycycline for three days. For western blots, cells were treated with the indicated amounts of Dasatinib (MedChem Express, HY-10181) for 4 hours and then bolted for total Src (Cell Signaling Technology, 2123T), Src-Tyr527 (Cell Signaling Technology, 2105T) and Src-Tyr461 (Cell Signaling Technology, 6943T). For SPT, BT MEFs were first stained with SNAP-JF549 (500 nM) and Halo-JF646 (1 nM) for 30 minutes. After washing, the cells were plated on fibronectin-coated cover-glasses and treated with 100 nM Dasatinib. After 4 hours, the cells were examined using TIRF microscopy.

Single molecule co-diffusion detection

To track individual molecules, low dye concentrations were used, so that only a sub-population of the target proteins (tagSrc and/or binder) were fluorescently labeled. All binder events on the membrane were assumed to have a corresponding tagSrc, even though the tagSrc in some cases would not be fluorescent. Therefore, when searching for co-diffusion events, we selected for all tagSrc trajectories that co-diffused (distance < 100 nm per frame) with another binder trajectory for at least five consecutive frames (100 ms) during their residence on the PM. This resulted in $n = 1094$ co-diffusion events over $n = 61$ cells.

Fixed cell PALM imaging

COS-7 cells were transiently transfected with Src-mGeosM for 12~16 hours and plated on fibronectin-coated coverglass for 4 hours. For fixation, cells were treated with 3.7% PFA for ~20 minutes at room temperature. Each cell was imaged for 10,000–20,000 frames.

PALM reconstruction was done using in-house MATLAB-based scripts. The cluster size was estimated with pair-correlation PALM analysis (Sengupta et al., 2011). Briefly, we first identified single molecule localizations (see *single molecule tracking* section) from all frames of the acquired movie to construct a superresolution map. Next, we manually chose regions of interests ($3 \mu\text{m} \times 3 \mu\text{m}$) from 7 cells for correlation analysis. The peaks of the autocorrelation function were measured to estimate cluster size.

Cluster detection and analyses

Cluster identification and refinement were based on the following steps: Track centroids, rather than whole trajectories, were used as the input to the tessellation process to avoid bias for longer-lived tracks and to avoid false-positive cluster detection due to repeated observation of a slow-moving molecule. Reducing the dataset to track centroids also allowed much more efficient computation. The polygon size threshold was obtained as described by Andronov et al. (2016): 50 realizations of randomly distributed points were subjected to Voronoi tessellation, and probability density functions of the experimental and mean simulated polygon sizes were computed. Their intersection defined the threshold. Next, tracks that diffused into proposed clusters were added, even if their centroids were not originally assigned (Figure S6D). Sets of tracks with large temporal separation, despite being spatially clustered, were split into separate assignments as follows (Figures 6B and S6E). A new molecule was typically observed at a cluster at least once every 4 s (> 90% of all recruitment events). Therefore, proposed clusters with longer time gaps between track appearances were split. To remove spurious clusters, we ignored clusters that had fewer than 10 tracks, clusters that contained 3 or more tracks at the same instant in time, clusters that were first observed within the first 4 s of imaging, and clusters that had multiple unconnected regions after thresholding at their half-maximal density.

To measure cluster sizes, we computed kernel density estimates (KDE) using the localizations associated with sets of clustered tracks. Gaussian kernels with optimized bandwidths were used (Bowman and Azzalini, 1997). The domain was padded out by $1 \mu\text{m}$ in each direction to avoid boundary artifacts, and calculations were performed on $10 \text{ nm} \times 10 \text{ nm}$ pixelated grids. After computing a KDE for each cluster, each density map was thresholded at 50% of its maximum to generate binary masks with areas and effective radii $r = \sqrt{A/\pi}$. Distributions of the corresponding areas for all clusters are provided in supplemental figures (Figures S6J and S6M). The main text figures (Figure 6G and 6I) show violin plots of bootstrapped median radii after $B = 100,000$ bootstraps with replacement. The violin plots were produced using `seaborn.violinplot` (v 0.10.1) (Waskom, 2021) in Python 3, using a kernel bandwidth of 1, and cutting the violin range to the range of the observed data. The sizes of slow and fast zones within clusters were computed by isolating slow (or fast) localizations, then repeating the KDE analysis as described above. Main components of this code are available at <https://github.com/mikepab/binder-tag/> and at <https://hahnlab.com>. Simulations and analyses were primarily performed using Linux systems (Longleaf cluster at UNC Chapel Hill, 2.50 GHz and 2.30 GHz Intel Processors), with some subsequent analyses conducted on a Macintosh computer (3.4 GHz Intel Processor).

Detecting enrichment of co-diffusion events in clusters

Co-diffusion events were annotated as either clustered or not by using both detected tagSrc clusters and detected binder clusters as references. This allows co-diffusion events to account for potentially undetected clusters, which may occur due to the existence of non-fluorescent tagSrc and binder. The percentage of cluster-associated co-diffusion events was then determined as an assessment of Src activity within detected clusters. As a null hypothesis, where clustering was unrelated to activity, randomized pairs of tagSrc and binder tracks ($n = 1094$ pairs to match the number of co-diffusion events) were selected, and the percentage of cluster-associated randomized events was determined. This randomization was performed 10 times, and the actual cluster-associated co-diffusion events were compared to the random simulation by a one-sample t test.

Cluster entry from cytoplasm versus plasma membrane

Cluster-associated tracks were considered recruited from the cytoplasm if their first frame was within the cluster boundary, as determined by the KDE map using 50% of the maximum density. To simulate random uniform recruitment, we first computed the “cluster extents,” defined by thresholding the KDE map by 5% of the maximum density. The cluster boundary was embedded within the cluster extents, and under uniform recruitment, tracks were equally likely to land throughout the cluster extents. Therefore, the predicted fraction of cytoplasm-recruited tracks for clusters with uniform recruitment was determined by dividing the area within the cluster boundary by the area of the cluster extents.

Analysis of the number of Src molecules in a cluster

Let k_{on_b} denote the rate at which a labeled binder molecule associates with a tagSrc molecule (either fluorescently labeled or not). k_{on_b} can be written as:

$$k_{on_b} = k'_{on_b} p_a$$

k'_{on_b} is the rate at which a labeled binder associates with an active tagSrc molecule and p_a is the probability that a tagSrc molecule is active and free of unlabeled binder. The rate at which a binder associates with a cluster k_{on_BT} can be written as:

$$k_{on_BT} = k'_{on_b} p_{a-c} N_{TS} = k_{on_bc} N_{TS}$$

where N_{TS} is the number of tagSrc in the cluster and $p_{a,c}$ is the probability that a tagSrc molecule in a cluster is active and free of unlabeled binder. To estimate $k_{on,b}$ requires analysis of co-diffusion events. That is, events in which labeled tagSrc and labeled binder are present at the same place and time. Specifically, we make use of co-diffusion events in which labeled tagSrc arrives followed by labeled binder (i.e., they do not arrive together). When a labeled tagSrc appears on the membrane, it can either dissociate with rate $k_{off,TS}$ or a labeled binder can bind to it. The probability that a labeled binder binds to the labeled tagSrc before it dissociates is:

$$p_c = \frac{k_{on,b}}{k_{on,b} + k_{off,TS}}$$

We can also estimate p_c from our single molecule data as the fraction of co-diffusion events N_{cd} out of the total observed number of labeled tagSrc molecules N_{TS} :

$$p_c = \frac{N_{cd}}{N_{TS}} = \frac{k_{on,b}}{k_{on,b} + k_{off,TS}}$$

From which we find

$$k_{on,b} = \frac{\frac{N_{cd}}{N_{TS}} k_{off,TS}}{1 - \frac{N_{cd}}{N_{TS}}}$$

Using the above expression with the values $N_{cd}/N_{TS} = 0.001$ and $k_{off,TS} = 3.5 \text{ s}^{-1}$ determined from the data, we find $k_{on,b} = 0.0035 \text{ s}^{-1}$. The probability that tagSrc is active might depend on whether tagSrc is part of cluster. The majority of co-diffusion events are not associated with clusters. Therefore, our estimate of $k_{on,b}$ may not apply to clusters. We can determine if the probability for tagSrc to be active varies in clusters in the following way. Note the rates $k_{on,b}$ and $k_{on,bc}$ are related through the relations

$$k_{on,bc} = p_{a,c} k'_{on,b}$$

$$k_{on,b} = p_a k'_{on,b}$$

Equating $k'_{on,b}$ in the two equations above produces:

$$k_{on,bc} = \frac{p_{a,c}}{p_a} k_{on,b}$$

Therefore, to compute $k_{on,bc}$ we need to estimate the ratio for the probability of Src molecules being active in a cluster versus being active when not identified as being part of cluster. We can estimate this quantity as the ratio of the relative number of co-diffusion events that occur in clusters to that of the relative number that were not identified as being associated with clusters:

$$f = \frac{p_{a,c}}{p_a} = \frac{\left(\frac{\text{co-diffusion events in tagSrc clusters}}{\text{number of clustered tagSrc tracks}} \right)}{\left(\frac{\text{co-diffusion events not identified as part of a cluster}}{\text{number of non-clustered tagSrc tracks}} \right)}$$

Using the above expression, we find $f = 2.5$. From which we have $k_{on,bc} = 2.5 k_{on,b} \approx 0.01 \text{ s}^{-1}$. From the distribution of arrival times for labeled binders in clusters, we estimate the rate at which binder associates with a cluster as $k_{on,BT} = 1.7 \text{ s}^{-1}$. Using this value and $k_{on,bc} = 0.01 \text{ s}^{-1}$, we estimate the number of tagSrc in a cluster to be $N_{TS} = k_{on,BT}/k_{on,bc} = 170$. From Western Blot analysis, we determined the ratio of WT Src to tagSrc to be roughly 1:5. Therefore the number of Src molecules in a cluster is roughly $1.2 N_{TS} \approx 200$. Using fixed cells, we can estimate the radius of a cluster to be 85 nm. If we assume a Src molecule has an effective radius of 3.5 nm, then approximately 450 Src molecules can fit in a cluster, assuming they are packed on a square lattice. Therefore, our estimate of 200 molecules appears reasonable. From our kinetic model, we estimate $p_a = 0.29$ from which we estimate $p_{a,c} = 3 \times p_a = 0.87$. Therefore, we can estimate the number of active Src molecules in a cluster to be on the order of $0.87 \times 200 = 174$.

Validation of cluster identification criterion

The results of our analysis above suggest the existence of Src clusters consisting of roughly 170 active Src molecules. However, to see individual molecules, it was necessary to label a small fraction of tagSrc and binder molecules. This means we rarely see multiple labeled tagSrc or multiple labeled binders appearing simultaneously in a cluster. Therefore, it is possible that the events designated as clusters actually resulted from a single long-lived binding site. This scenario would represent a false positive. Even though our analysis above suggests that clusters of approximately 200 Src molecules, if there were many more single Src binding sites

or single tagSrc molecules than clusters, the probability of a false positive might be reasonably large. We address this issue by constructing an upper bound for the probability P_C of observing at least N_E sequential binder binding events to a single tagSrc molecule in time T_C . Our definition of cluster requires $N_E = 10$. The value of T_C represents the characteristic lifetime of a cluster. As an estimate for T_C , we use the median cluster lifetime estimated from our data $T_C = 10$ s.

To begin our analysis, note that our criterion for a cluster is at least 10 binding and dissociation events in a row. Let $f(t)$ represent the probability density for the time for a binding event followed by a dissociation event to occur. Then if the random variable T represent the time for N_E such events to occur. We can write T as:

$$T = \sum_{i=1}^{N_E} \tau_i$$

where τ_i represents the time for a single binding and dissociation event to occur. Because the τ_i are independent events, we can write their joint distribution as

$$F(\bar{\tau}) = \prod_{i=1}^{N_E} f_i(\tau_i)$$

Using this distribution, we compute the probability that $T \leq T_C$ as:

$$\Pr[T \leq T_C] = \int_0^{T_C} \int_0^{T_C - \tau_{N_E}} \int_0^{T_C - \tau_{N_E} - \tau_{N_E - 1}} \dots \int_0^{T_C - \sum_{i=2}^{N_E} \tau_i} \prod_{i=1}^{N_E} f_i(\tau_i) d\tau_{N_E} \dots d\tau_1$$

Note the following relation holds from the above equation:

$$\Pr[T \leq T_C] \leq \left(\int_0^{T_C} f(\tau) d\tau \right)^{N_E}$$

Therefore, if we can compute $f(t)$, we can use the expression above to put an upper bound on the probability for observing a sequence of N_E or more binding/unbinding events within time T_C . Computing $f(t)$ is a first passage time problem. The starting point for the calculation is the following set of differential equations:

$$\frac{dp_0}{dt} = -k_{on}p_0$$

$$\frac{dp_1}{dt} = k_{on}p_0 - k_{off}p_1$$

where k_{on} is the rate at which a labeled molecule associates with a binding partner and k_{off} is the rate at which it dissociates. Solving the above equations with the initial conditions $p_0 = 1$ and $p_1 = 0$ yields

$$p_0 = e^{-k_{on}t}$$

$$p_1 = \frac{k_{on}}{k_{off} - k_{on}} (e^{-k_{on}t} - e^{-k_{off}t})$$

From which $f(t)$ can be computed as

$$f(t) = - \left(\frac{dp_0}{dt} + \frac{dp_1}{dt} \right) = k_{off}p_1 = \frac{k_{off}k_{on}}{k_{off} - k_{on}} (e^{-k_{on}t} - e^{-k_{off}t})$$

Integrating $f(t)$ produces

$$\int_0^{T_C} f(\tau) d\tau = 1 + \frac{k_{off}k_{on}}{k_{off} - k_{on}} \left(\frac{e^{-k_{off}T_C}}{k_{off}} - \frac{e^{-k_{on}T_C}}{k_{on}} \right)$$

Note that we have estimated $k_{on} = k_{on,B} = 0.004 \text{ s}^{-1}$ and from our data we estimate $k_{off} = 1.74 \text{ s}^{-1}$. Because $T_C = 10 \text{ s}$, $\exp[-k_{off} T_C] \ll 1$ and $k'_{on,b} T_C \ll 1$. We can use these relations to approximate the above expression as:

$$\int_0^{T_C} f(\tau) d\tau \approx 1 - \frac{k_{off}}{k_{off} - k_{on}} (1 - k_{on} T_C) = 1 - \frac{1}{1 - \frac{k_{on}}{k_{off}}} (1 - k_{on} T_C)$$

$$\int_0^{T_C} f(\tau) d\tau \approx 1 - \left(1 + \frac{k_{on}}{k_{off}}\right) (1 - k_{on} T_C) \approx k_{on} T_C - \frac{k_{on}}{k_{off}}$$

From which we have:

$$\Pr[T \leq T_C] \leq \left(\int_0^{T_C} f(\tau) d\tau \right)^{N_E} \approx \left(k_{on} T_C - \frac{k_{on}}{k_{off}} \right)^{N_E} \leq (k_{on} T_C)^{N_E} \approx 10^{-14}$$

A simple interpretation of the above result is that $k_{on} T_C$ is roughly the probability for a tagSrc to bind within time T_C . Therefore, the probability of seeing N_E sequential binding/unbinding events must be less than the probability of seeing N_E binding events in time T_C . Assume there are 10^6 tagSrc molecules and all of them are bound to the membrane. A typical experiment lasts for $T_{exp} = 10 \text{ min}$ or 600 s . Therefore, there are $N_c = 10^6 T_{exp} / T_C \approx 10^9$ possible chances for a false positive. Given this large number, we still do not expect to see any false positives, $p = N_c 10^{-14} \approx 10^{-5}$. We conclude that our criterion of 10 events to identify clusters is conservative.

Stochastic model for cluster kinetics

The above analysis demonstrates that the probability of misidentifying a single binding site as a cluster is small and that clusters likely consist of around 200 tagSrc molecules. However, it does not address the probability of a false negative or the accuracy of the experimentally determined median cluster lifetime. Therefore, to further analyze cluster kinetics, we constructed the following stochastic model. The cluster lifetime is assumed to be an exponentially distributed random variable characterized by its mean $1/k_{lt}$. During the lifetime of the cluster, labeled tagSrc molecules bind with rate $k_{on,tS}$ and dissociate with rate $k_{off,tS}$. We focus on tagSrc clusters, because when a labeled binder leaves the membrane, it is not clear if this was due to the binder dissociating from tagSrc or tagSrc dissociating from the membrane. Because clusters consist of approximately 200 tagSrc molecules, we assume that $k_{on,tS}$ does not depend on the number of labeled tagSrc molecules present in the cluster. To simplify the notation presented below, we drop the tS in the subscripts of $k_{on,tS}$ and $k_{off,tS}$.

To be considered an experimentally detected cluster, the cluster has to satisfy two criteria: 1) no more than two labeled tagSrc can be present in the cluster at any given time and 2) at least 10 labeled tagSrc binding/unbinding events must be observed before the cluster disassembles. Let $N(t)$ represent the number labeled tagSrc in the cluster at time t . Then the first criterion requires that $N(t) \leq 2$ throughout the whole cluster lifetime. This criterion is consistent with the way the experimental data were collected.

We define a “binding/unbinding” event as follows. The starting time for a binding/unbinding event T_{start} is defined as the time when $N(t)$ transitions from $1 \rightarrow 0$ and the event continues until time T_{end} when the next $1 \rightarrow 0$ transition occurs. Because binding and unbinding events are stochastic process, the time interval $T = (T_{start}, T_{end})$ is also a random process. The experimentally determined distribution for cluster binding/unbinding events is given in Figure 6C. We can compute this distribution from our model as follows. Let $p_i(t)$ denote the probability that a cluster contains i labeled tagSrc molecules at t . The functions $p_i(t)$ satisfy the following master equation:

$$\frac{dp_0}{dt} = -k_{on} p_0$$

$$\frac{dp_1}{dt} = -(k_{on} + k_{off}) p_1 + k_{on} p_0 + 2k_{off} p_2$$

$$\frac{dp_2}{dt} = -(k_{on} + 2k_{off}) p_2 + k_{on} p_1$$

with the initial conditions $p_0(0) = 1$, $p_1(0) = 0$ and $p_2(0) = 0$. Note that the above process terminates when either a third binding event occurs, which happens with rate $k_{on} p_2(t)$, or a successful binding/unbinding event occurs, which happens with rate $k_{off} p_1(t)$. The

probability density for the time at which the above process terminates is given by $f(t) = k_{off} p1(t) + k_{on} p2(t) = f_{suc}(t) + f_{fail}(t)$, where the first term represents the times that a successful binding/unbinding event occurs and the second term represents the times for when the criterion $N(t) \leq 2$ is not met. The model equations were solved symbolically using Mathematica.

The second criterion is that 10 binding/unbinding events must occur before the cluster disassembles. Cluster disassembly events and binding/unbinding events are assumed to be independent. Therefore, the joint distribution for the times when these events occur is $F(t_1, t_2) = f_{suc}(t_1) \times f_d(t_2)$. We assume the cluster lifetime distribution $f_d(t)$ is exponential, $f_d(t) = k_{lt} \exp(-k_{lt} t)$. This would be the case if there was one rate limiting step for cluster disassembly. The average cluster lifetime is given by $1/k_{lt}$. From these considerations we compute the probability of a successful binding/unbinding event:

$$P_{suc} = \int_0^{\infty} f_{suc}(t_2) \int_{t_2}^{\infty} f_d(t) dt dt_2 = \frac{k_{off} k_{on} (k_{lf} + 2k_{off} + k_{on})}{(k_{lf} + k_{on}) (k_{lf}^2 + 3k_{lf} k_{off} + 2k_{off}^2 + 2k_{lf} k_{on} + k_{off} k_{on} + k_{on}^2)} \quad (\text{Equation 1})$$

and the average duration of a successful binding/unbinding event:

$$T_{Avg} = \frac{1}{P_{Suc}} \int_0^{\infty} t_2 f_{suc}(t_2) \int_{t_2}^{\infty} f_d(t) dt dt_2 \quad (\text{Equation 2})$$

$$T_{Avg} = \frac{(k_{off} - k_{on})(k_{off} + 8k_{on})((2k_{lt} + k_{off})(k_{lt} + 2k_{off})^2 + 2(3k_{lt}^2 + 9k_{lt}k_{off} + 4k_{off}^2)k_{on} + 3(2k_{lt} + 3k_{off})k_{on}^2 + 2k_{on}^3)}{(k_{lt} + k_{on})(k_{lt} + 2k_{off} + k_{on})(k_{off}^2 + 7k_{off}k_{on} - 8k_{on}^2)(k_{lt}^2 + 3k_{lt}k_{off} + 2k_{off}^2 + 2k_{lt}k_{on} + k_{off}k_{on} + k_{on}^2)}$$

The probability of failure because $N(t) > 2$, P_{F1} is:

$$P_{F1} = \int_0^{\infty} f_{fail}(t_2) \int_{t_2}^{\infty} f_d(t) dt dt_2$$

$$P_{F1} = \frac{k_{on}^3}{(k_{lf} + k_{on})(k_{lf}^2 + 3k_{lf}k_{off} + 2k_{off}^2 + 2k_{lf}k_{on} + k_{off}k_{on} + k_{on}^2)}$$

The probability of failure because the cluster disassembles before a successful binding/unbinding event P_{F2} is:

$$P_{F2} = \int_0^{\infty} f_d(t_2) \int_{t_2}^{\infty} (f_{fail}(t) + f_{suc}(t)) dt dt_2$$

$$P_{F2} = \frac{k_{lf} (k_{lf}^2 + 2k_{off}^2 + 3k_{on}k_{off} + 3k_{on}^2 + 3k_{lf}(k_{off} + k_{on}))}{(k_{lf} + k_{on})(k_{lf}^2 + 3k_{lf}k_{off} + 2k_{off}^2 + 2k_{lf}k_{on} + k_{off}k_{on} + k_{on}^2)}$$

Note that $P_{Suc} + P_{F1} + P_{F2} = 1$. Because binding/unbinding events are independent, the probability of cluster consisting of n binding/unbinding events is:

$$P_n = P_{suc}^n P_{F2} \quad (\text{Equation 3})$$

Note that the sum of P_n over all n does not equal one, because it does not include events in which more than two labeled tagSrc appeared. There are three experimental datasets that the model should reproduce: 1) the probability distribution for the number of tracks per cluster, 2) the distribution of cluster lifetimes, and 3) the distribution for the time for binding/unbinding events (Figure 6C). We describe how these datasets can be used to put constraints on the model parameters. Using Equation 3 to take the natural log of P_n , we find:

$$\ln(P_n) = n \ln(P_{suc}) + \ln(P_{F2})$$

Therefore, we can estimate P_{Suc} by fitting a line to the log of the experimentally determined distribution for track number per cluster (Figure S6F). From this we find $P_{suc} = \exp(-0.105) = 0.9$. To estimate T_{avg} , we use the following reasoning. Let M = the minimum track

threshold to be considered a cluster. Let T_M = the average cluster life time using a threshold of M . Then the following relation holds between the T_M 's:

$$T_{M+1} = T_M + T_{Avg}$$

which implies:

$$T_M = T_{Avg}M + T_0$$

Therefore, we can estimate T_{avg} by fitting a line to the average cluster lifetime as a function of M (Figure S6G). Doing this we, find $T_{avg} = 0.62$ s and $T_0 = 5.8$ s. Note that to fit a line to the average cluster life time we started with a minimum value of $M = 9$. The deviation from linearity for small values of M likely occurs because clusters have a finite minimum lifetime (i.e., the cluster lifetime does not follow an exponential distribution at short times). The fraction of tagSrc clusters that are successfully identified is:

$$P_{SI} = \sum_{m=10}^{\infty} p_{suc}^m p_{F2}$$

and the fraction of clusters that fail because 3 or more tagSrc are present simultaneously is:

$$P_F = \sum_{m=0}^{\infty} p_{suc}^m p_{F1} \tag{Equation 4}$$

From the data we find P_F to be between 0.4-0.8. We used the constraints on p_{suc} , T_{avg} and P_F to determine values for the model parameters as follows: we picked a value of k_{on} and then use Equations 1 and 2 to find k_{off} and k_{it} . We then used Equation 4 to evaluate P_F . The range for the values of k_{on} that produced P_F values in 0.4-0.8 range was 2.1-2.4 s^{-1} . For this range of values P_F ranged from between 0.41-0.82, k_{off} ranged between 5.0 s^{-1} , P_{SI} ranged between 0.2-0.06, and k_{it} ranged between 0.095-0.029 s^{-1} . The range for k_{it} corresponds to a range of 7.3-23.9 s for the median cluster lifetime. To validate our approach, we ran stochastic simulations using $k_{on} = 2.2$ s^{-1} , $k_{off} = 5.1$ s^{-1} , and $k_{it} = 0.049$ s^{-1} . The model showed excellent agreement with the experimental distributions for the number of tracks per cluster, observed cluster lifetime, and binding/unbinding times (Figure 6C).

Finally, to investigate the sensitivity of the model results on the choice of parameter values, we performed a systematic search of parameter space. We swept over $k_{on} = 0.9$ -3.4 (increment 0.05), $k_{off} = 3$ -21 (increment 0.5), and $k_{liffe} = 0.01$ -0.51 (increment 0.01), producing 90,000 parameter sets. For each parameter set, 200,000 realizations of the stochastic model were numerically solved using the Gillespie algorithm. The probability distribution for a successful binding/unbinding event was computed analytically in Mathematica as:

$$f_{B/U}(t) = \frac{1}{P_{SUC}} f_{suc}(t) \int_t^{\infty} f_d(t_2) dt_2$$

To score parameter sets, we calculated mean-squared errors between the model results and the experimentally measured distributions for: 1) the number of tracks per cluster, 2) cluster lifetime, and 3) binding/unbinding time. Furthermore, we constrained our simulations based on the observed low frequency of tagSrc cluster and Binder cluster co-localization as follows. The cluster co-localization probability is estimated as $P_{coloc} = P_{SI}^2$, where we have assumed that the probability of successfully observing a Binder cluster is equal to that of tagSrc cluster. We made this assumption because the distributions for the number of tracks per cluster, cluster lifetime and binding/unbinding time were similar for tagSrc and Binder clusters. We only accepted parameter sets for which $P_{coloc} \leq 0.015$, or a less than 1.5% probability of cluster colocalization. Finally, we required P_F to be between 0.4-0.8 as above. We accepted all parameter sets scoring in the top 5th percentile (Figures 6C and 6D). The effect of selecting different percentile thresholds is shown in Figures S6H and S6I.

Mathematical modeling of SPT kinetics

The continuous-time Markov chain model of Src regulation was simulated using a discrete time-step simulation with four states: (1) closed tagSrc at the plasma membrane, (2) open tagSrc at the plasma membrane, (3) open tagSrc with binder at the plasma membrane, and (4) an absorbing state representing translocation into the cytosol. The transition probability matrix is:

$$P = \begin{bmatrix} P_{aa} & 1 - \exp(-k_1 \Delta t) & 1 - \exp(-k_5 \Delta t) & 1 - \exp(-k_7 \Delta t) \\ 1 - \exp(-k_2 \Delta t) & P_{bb} & 1 - \exp(-k_3 \Delta t) & 1 - \exp(-k_8 \Delta t) \\ 1 - \exp(-k_6 \Delta t) & 1 - \exp(-k_4 \Delta t) & P_{cc} & 1 - \exp(-k_8 \Delta t) \\ 0 & 0 & 0 & 1 \end{bmatrix},$$

where Δt is the simulated time step, and P_{aa}, P_{bb}, P_{cc} were calculated such that the rows summed to one. The timestep was selected such that $P_{ij} < 0.1$, for $i \neq j$. A Markov chain simulation using a particular parameter vector $\vec{\theta}$ resulted in a sequence of states $\vec{s} = \{s_1, s_2, \dots, s_T\}$ where each s_i is state A, B, or C, and the final state is state D. Analysis of the sequence \vec{s} yielded process waiting times, track lifetimes, and a co-diffusion sequence. These simulations were repeated five thousand times using each of the three non-absorbing states as initial conditions to generate distributions for each parameter vector $\vec{\theta}$. The relative proportion of events starting from the three states was weighted by the additional parameters f_1, f_2 , and f_3 , which summed to one. Of all co-diffusion events, 24% started with both tagSrc and binder together, so f_3 was fixed to 0.24. Furthermore, two parameters were fixed: k_3 and k_5 . First, the process represented by k_5 is activation of labeled tagSrc by labeled binder, and the corresponding rate was fixed to zero because binder overexpression did not induce aberrant Src activation (Figures S3F and S3G). Next, the process represented by k_3 is the association between labeled tagSrc and labeled binder. Because of low labeling density, this process occurs infrequently, so the estimated value of this rate is very small ($k_{on,b} = 0.004 \text{ s}^{-1}$, see **Analysis of the number of Src molecules in a cluster**). However, by selecting for co-diffusion events, k_3 becomes determined instead by overall dissociation rate of tagSrc from the membrane. This is estimated to be 3.47 s^{-1} from clustered track lifetime data (Figure S6Q). Therefore, we optimized the parameter vector $\vec{\theta} = \{k_1, k_2, k_4, k_6, k_7, k_8, f_1\}$. Simulated trajectories $\{\vec{s}_1, \vec{s}_2, \dots, \vec{s}_n\}$ were analyzed to produce simulated distributions with the same constraints as the experimental data: tracks shorter than 12 frames (240 ms) were ignored; tracks where binder arrived, departed, then arrived again were ignored; and unless binder was present for at least 12 consecutive frames, the track was not considered a co-diffusion event.

Two-step parameter inference of SPT kinetics

A two-step approach was used to search parameter space globally, then locally. We used an evolutionary algorithm (EA) (Fortin et al., 2012) optimization followed by Delayed Rejection Adaptive Metropolis-Markov Chain Monte Carlo (DRAM-MCMC) (Haario et al., 2006; Miles, 2019). For the EAs, a single evolution consisted of 100 parameter sets (“individuals”) that competed, mated, and mutated over 100 cycles (“generations”). Three-individual tournaments were used for mating, where the two best-fitting individuals mixed parameters to produce a new individual, while the worst-fitting individual was removed. Crossover and mutation rates were set to 0.5 and 0.1, respectively. The initial parameters for EA optimization were based on exponential fits to the data. For DRAM-MCMC, the single best parameter set from the EA runs was used to initialize fitting; of 10,000 total steps taken, the first 5,000 steps were thrown away as burn-in. DRAM-MCMC inputs for S20 and N0 were both set to 0.045, leading to acceptance rates near 23.4% (Haario et al., 2006). Three independent chains were simulated, and chain convergence was verified using Geweke and Gelman-Rubin diagnostics (Gelman and Rubin, 1992; Geweke, 1992). For both steps, we used the score function:

$$\begin{aligned} \text{Score} = & \text{MSE}(\text{process_i}) + \text{MSE}(\text{process_ii}) + \text{MSE}(\text{process_iii}) + \text{MSE}(\text{process_iv}) \\ & + \text{MSE}(\text{tagSrc_lifetime_codiffuse}) + \text{MSE}(\text{tagSrc_lifetime_all}) \\ & + \text{MSE}(\text{binder_lifetime_codiffuse}) + \text{MSE}(\text{codiffusion_sequence_category}), \end{aligned}$$

where the $\text{MSE}(\bullet)$ is the mean-squared error between experimental and simulated distributions.

For model validation, we simulated the kinetic model with $\vec{\theta}_{val} = \{k_1 = 6, k_2 = 7, k_4 = 2, k_6 = 1, k_7 = 13, k_8 = 0.17, f_1 = 0.13\}$. The number of simulated observations were closely matched to the number of experimental observations for the four measurable process times. The initial 6,000 DRAM-MCMC steps were discarded as burn-in, and the following 5,000-step chain was analyzed. S20 and N0 were both set to 0.035 to tune the acceptance ratio. We verified convergence in these chains as before. We were able to rediscover the parameters k_4, k_6, k_7 , and f_1 within 1 SD of the mean, and k_1, k_2 , and k_8 within 2 SDs of the mean (Figures S7D and S7E). The variance of the k_1, k_2 , and k_7 distributions were poorly constrained in both the validation and experimental fits. Because we cannot observe the interconversion between closed and open tagSrc in the absence of binder, we expected k_1 and k_2 to be poorly constrained. However, we can infer the relative proportions of closed and open tagSrc, and consistent with this the ratio $k_1/(k_1+k_2)$ is better constrained (Figure S7F).

Main components of this code are available at <https://github.com/mikepab/binder-tag/>. Both the EA and the DRAM-MCMC fits were conducted using Linux systems (Longleaf cluster at UNC Chapel Hill, 2.50 GHz and 2.30 GHz Intel Processors), each step taking at minimum 2-3 days per CPU, with subsequent analyses conducted on a Mac (3.4 GHz Intel Processor).

QUANTIFICATION AND STATISTICAL ANALYSIS

GraphPad Prism 8.4.3, MATLAB (Mathworks) and seaborn (<https://seaborn.pydata.org/index.html>) were used to generate the graphs and perform statistical analysis. Significance was typically judged by either unpaired or paired Student's t tests, or by one-way ANOVA with Tukey-Kramer correction for multiple hypotheses, where * $p < 0.05$, ** $p < 0.01$, *** $p < 0.001$, **** $p < 0.0001$. In Box-and-whisker plots, the box always extends from the 25th to 75th percentiles, the line in the middle of the box is plotted at the median, the whiskers are drawn down to the 10th percentile and up to the 90th. Points below and above the whiskers are drawn as individual points.

Supplemental figures

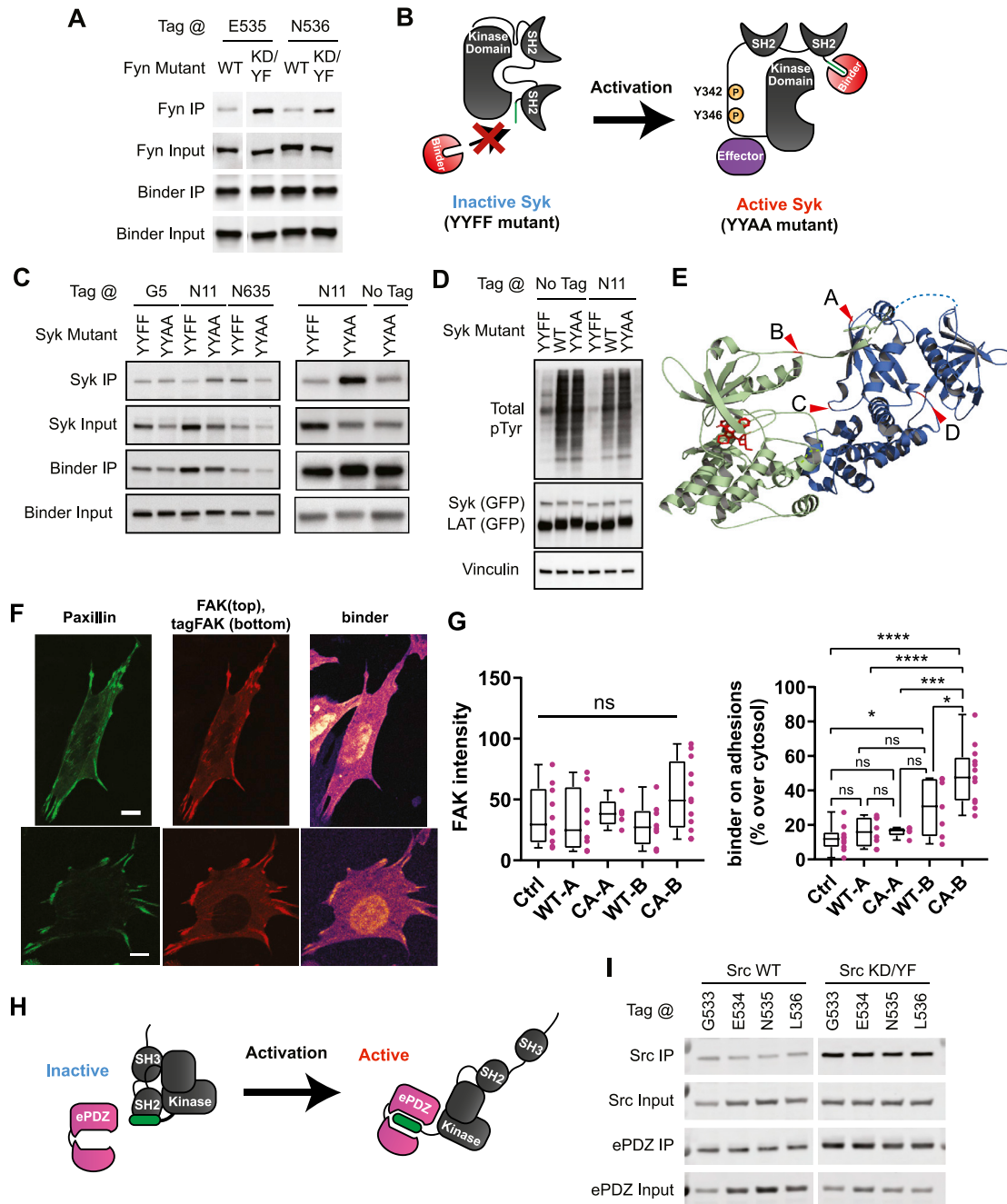


Figure S1. Development of binder/tag Fyn, binder/tag Syk, binder/tag FAK, and an orthogonal binder/tag pair, related to Figure 2

(A) Comparing SspB interaction for tagFyn versus a tagFyn open conformation mutant (Y527F/K299M, KD/YF). Co-immunoprecipitation of tagFyn and FLAG-SspB (binder). SsrA was inserted after the indicated residue. KD: kinase-dead.

(B) Schematic of binder/tag Syk. Two tyrosine sites (Y342 and Y346) were mutated to either phenylalanine (rendering closed tagSyk, YYFF) or alanine (rendering open tagSyk, YYAA).

(C) Comparing SspB interaction of tagSyk closed conformation and open conformation mutants (YYAA versus YYFF respectively). Co-immunoprecipitation of FLAG-SspB with Syk mutants (with and without tag insertion). The tag was inserted at the indicated positions (*top*). The insertion site with the best dynamic range (N11) was replicated, along with Syk without the tag insertion as a control.

(legend continued on next page)

(D) Syk with and without the tag insertion at N11 was expressed in LinXE cells and whole-cell lysates were immunoblotted for the indicated proteins.

(E) Crystal structure of the FERM (blue) and kinase (green) domains of FAK (PDB: 2J0J). Red arrows indicate the four tested SsrA insertion sites (A: R35, B: D405, C: Y128, D: S47). The N-terminal FERM domain is attached to the central kinase domain via a linker chain. The FERM domain binds and inhibits the kinase domain until phosphorylation by Src sets in motion a series of conformational changes that culminate in catalytic activity (Lietha et al., 2007).

(F) MEFs stably expressing binder-SNAP-tag (labeled with dye JF646) were transiently transfected with the adhesion marker Paxilin-EGFP and constitutively active mutants of either FAK-mCherry or tagFAK-mCherry (Karginov et al., 2010; Lietha et al., 2007). The top row shows control FAK lacking the tag. Two of four insertion sites retained adhesion localization (sites A and B), and both showed colocalization of tagFAK and binder (e.g., bottom row, showing site b). Binder largely distributed in the cytosol and was recruited to adhesions only when interacting with tagFAK.

(G) Ctrl: FAK-mCherry; A, B: insertion sites shown in (E). CA: constitutively active FAK. Left, Intensity of FAK on adhesions: tag insertion at sites A and B didn't alter FAK localization to adhesions. Right, intensity of binder at adhesions: The activating mutation increased focal adhesion localization of binder only for site b, indicating conformation-dependent binding for this tag position. Control: 810 adhesions from 10 cells; WT-A: 612 adhesions from 8 cells; CA-A: 464 adhesions from 5 cells; WT-B: 697 adhesions from 8 cells; CA-B: 692 adhesions from 12 cells. See [STAR Methods](#).

Further development of this FAK analog as a biosensor would include testing for perturbation of the pathway or cell behavior under study.

(H) Schematic of orthogonal binder/tag Src based on ePDZ and ARVCF.

(I) Co-immunoprecipitation of Src-ARVCF and FLAG-ePDZ using anti-FLAG antibody. Wild-type versus open conformation Src mutant (Y527F/D388R, or KD/YF). The ARVCF peptide was inserted after the indicated residues. KD: kinase-dead.

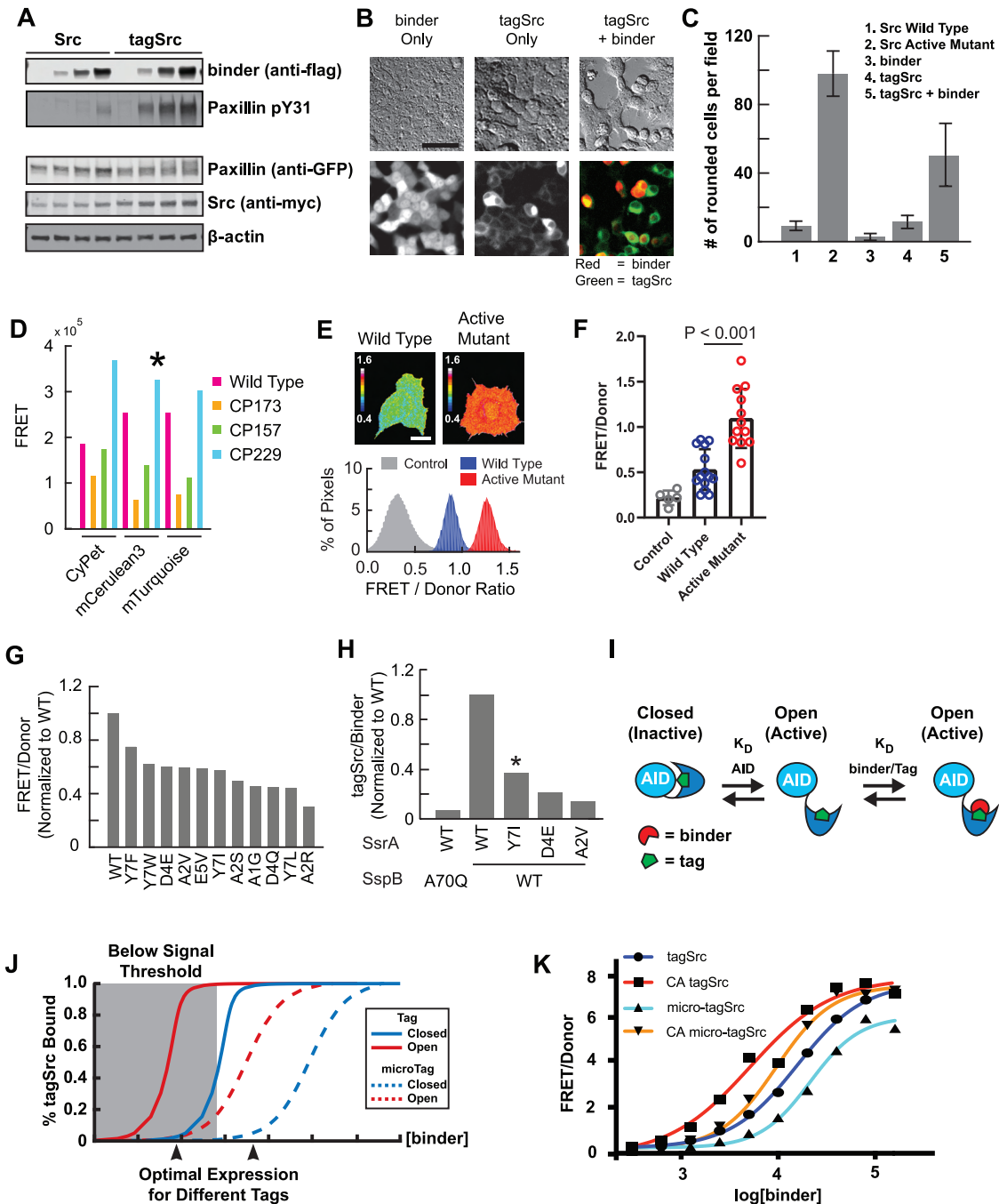


Figure S2. Optimization and modeling of FRET-based binder/tag biosensors, related to Figure 3

(A) LinXE cells were co-transfected with paxillin and either Src or tagSrc. Whole-cell lysates were immunoblotted for indicated proteins.
 (B) Representative images of LinXE cells expressing tagSrc-GFP and binder-mCherry. Cells were imaged with DIC (top) and epifluorescence (bottom).
 (C) Only constitutively active Src and tagSrc combined with binder caused cell rounding. Scale bar: 50 μ m.
 (D) Screening different combinations of CFP variants (CyPet, mCerulean3, and mTurquoise) and YPet circular permutants (wild-type, CP173, CP157, CP229). TagSrc and SspB were attached to CFP and YFP, respectively. FRET emission is displayed on the y axis. Star indicates optimized FRET pair (mCerulean3 and YPet CP229).
 (E) MEF cells expressing FRET biosensor based on tagSrc or tagSrc Y527F active mutant (top). TagSrc and SspB were expressed at approximately equal levels as measured by CFP and YFP emission intensities per unit area. Color scale indicates FRET/CFP emission values. A histogram showing FRET/CFP ratio values for each cell is shown at bottom. Control cells were transfected with tagSrc-mCerulean and yPet-cp229. Scale bar: 10 μ m.
 (F) FRET/CFP emission values for MEF cells expressing wild-type (n = 14) or Y527F active mutant (n = 12) tagSrc FRET biosensor. Control cells were transfected with tagSrc-mCerulean and yPet-cp229 (n = 5). p value was calculated with an unpaired two-sample Student's t test.

(legend continued on next page)

(G) Initial screen to identify tag mutants with reduced affinity. Normalized FRET/CFP emission values for LinXE cells expressing the tagSrc FRET biosensor with the indicated tag mutants are shown. TagSrc and SspB were expressed at approximately equal levels as measured by average CFP and YFP emission intensities. This initial screen was carried out once.

(H) Co-immunoprecipitation of tagSrc mutants and FLAG-SspB using anti-FLAG antibody. Reduced affinity SspB (A70Q) used as a control is in the left lane. Other lanes use WT SspB. Band densities were quantified, and normalized tagSrc/SspB is displayed on the y axis ($n = 1$).

(I) A model of SspB binding to SsrA-tagged proteins. The effect of AID engagement on SspB binding was incorporated by applying the Schild model of competitive antagonism (Colquhoun, 2007; Schild, 1947).

(J) After specifying the Src concentration and AID affinity, the SsrA/SspB affinity determined the SspB concentration needed to bind a given percent of tagSrc. For inactive tagSrc, AID affinity is high (Roskoski, 2004), so AID competes strongly with SspB. For active tagSrc, AID affinity is low and competition is weaker. In our past experience with GTPase pathways roughly 200-800 nM biosensor has been required for FRET imaging (Azoitei et al., 2019; Hodgson et al., 2016; Machacek et al., 2009; Marston et al., 2020; Nalbant et al., 2004; Pertz et al., 2006; Zawistowski et al., 2013). The model indicates that at these concentrations we should reduce the affinity of SspB to prevent activation of tagSrc.

(K) FRET for a fixed concentration of tagSrc or micro-tagSrc, with varying levels of SspB. Lowering the affinity of SsrA shifted the binding isotherms as predicted.

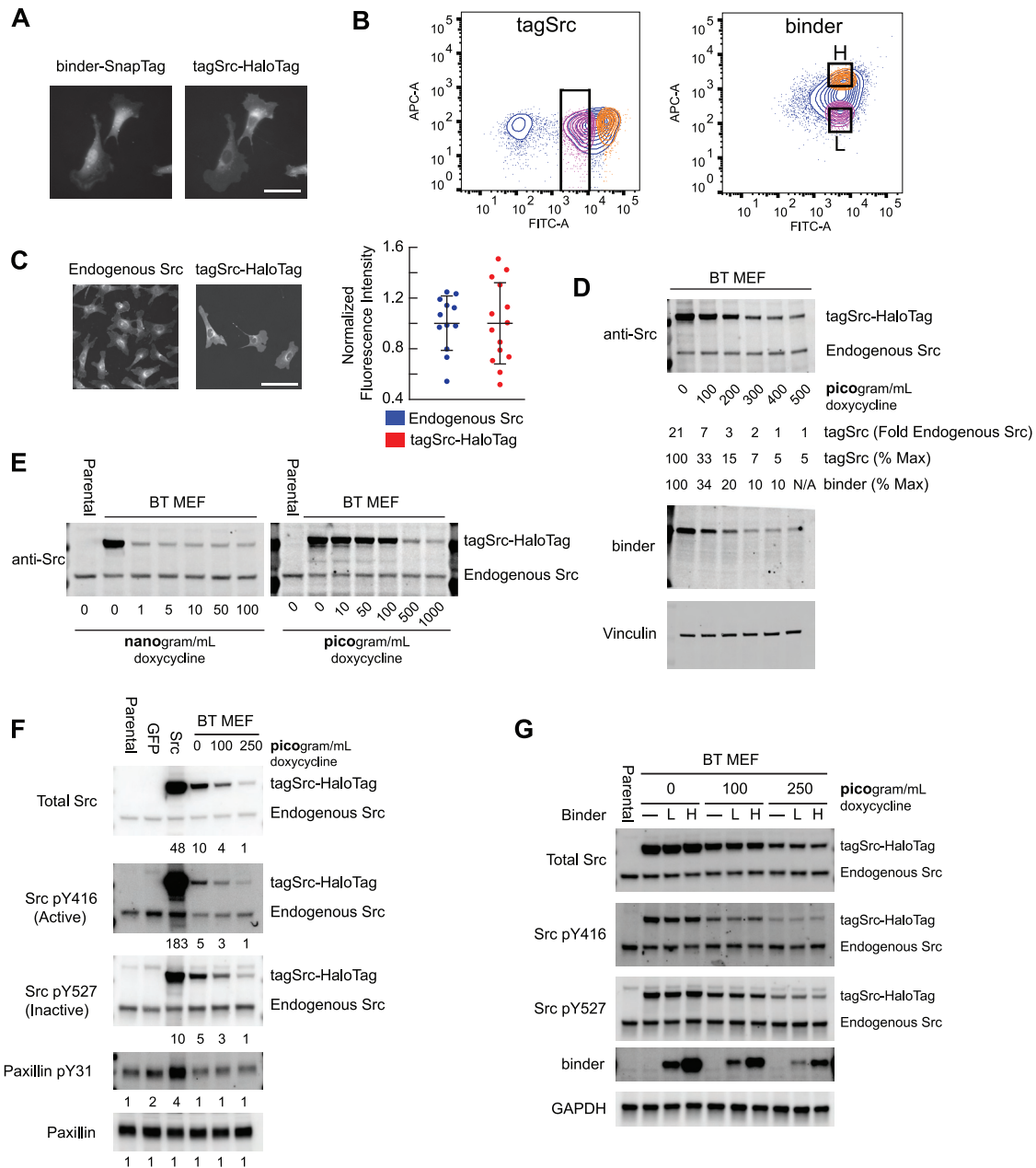


Figure S3. Generation of MEFs stably expressing tagSrc and binder, related to Figure 4

(A) MEF cells stably expressing tagSrc-HaloTag and binder-Snap-tag were labeled with Oregon Green (HaloTag ligand) and MeroSnap (SNAP-tag ligand). Cells were imaged using epifluorescence microscopy.

(B) Populations with different expression levels in BT MEF cells were selected by flow cytometry. Cells were selected for low expression of tagSrc (left), with high or low binder expression (right). Scale bar: 50 μ m.

(C) Immunofluorescence of parental MEF cells stained for endogenous Src (left). BT MEF cells stably expressing tagSrc-HaloTag labeled with Oregon Green (middle). Cells were imaged using epifluorescence microscopy. Quantification of normalized fluorescence intensity for tagSrc-HaloTag ($n = 14$) or endogenous Src ($n = 12$) (right). Scale bar = 50 μ m.

(D) Whole-cell lysates of BT MEF cells were immunoblotted for the indicated proteins. Doxycycline concentration was titrated to control the level of expression. TagSrc-HaloTag band density was quantified and normalized to either endogenous Src or fully induced tagSrc-HaloTag.

(E) Whole-cell lysates of BT MEF and parental MEF cells were immunoblotted for Src. Doxycycline concentration was titrated to control the level of expression.

(F) Whole-cell lysates of BT MEF, parental MEF cells, and electroporated parental MEF cells (GFP and Src) were immunoblotted for the indicated proteins. Normalized band densities were quantified. TagSrc-HaloTag and phospho-tagSrc-HaloTag were normalized to endogenous Src in the top three rows (Src pY416, Src pY527). Phospho-paxillin was normalized to paxillin in the bottom two rows (Paxillin pY31).

(legend continued on next page)

Expression up to 10-fold endogenous Src did not alter Src or paxillin phosphorylation. In contrast, expression at 40-fold endogenous reduced the inactivating phosphorylation at Src Y527, increased the activating phosphorylation at Src Y416, and increased phospho-paxillin (F). We therefore carried out all following biological studies at < 7-fold endogenous Src, with SspB at the minimum necessary expression level.

(G) Whole-cell lysates of binder-Low and binder-High BT MEFs and parental MEF cells were immunoblotted for the indicated proteins. Doxycycline concentration was titrated to control the level of expression. MEFs expressing high and low amounts of SspB within our optimized concentration range (B, right panel) did not display significantly different Src phosphorylation relative to MEFs lacking SspB.

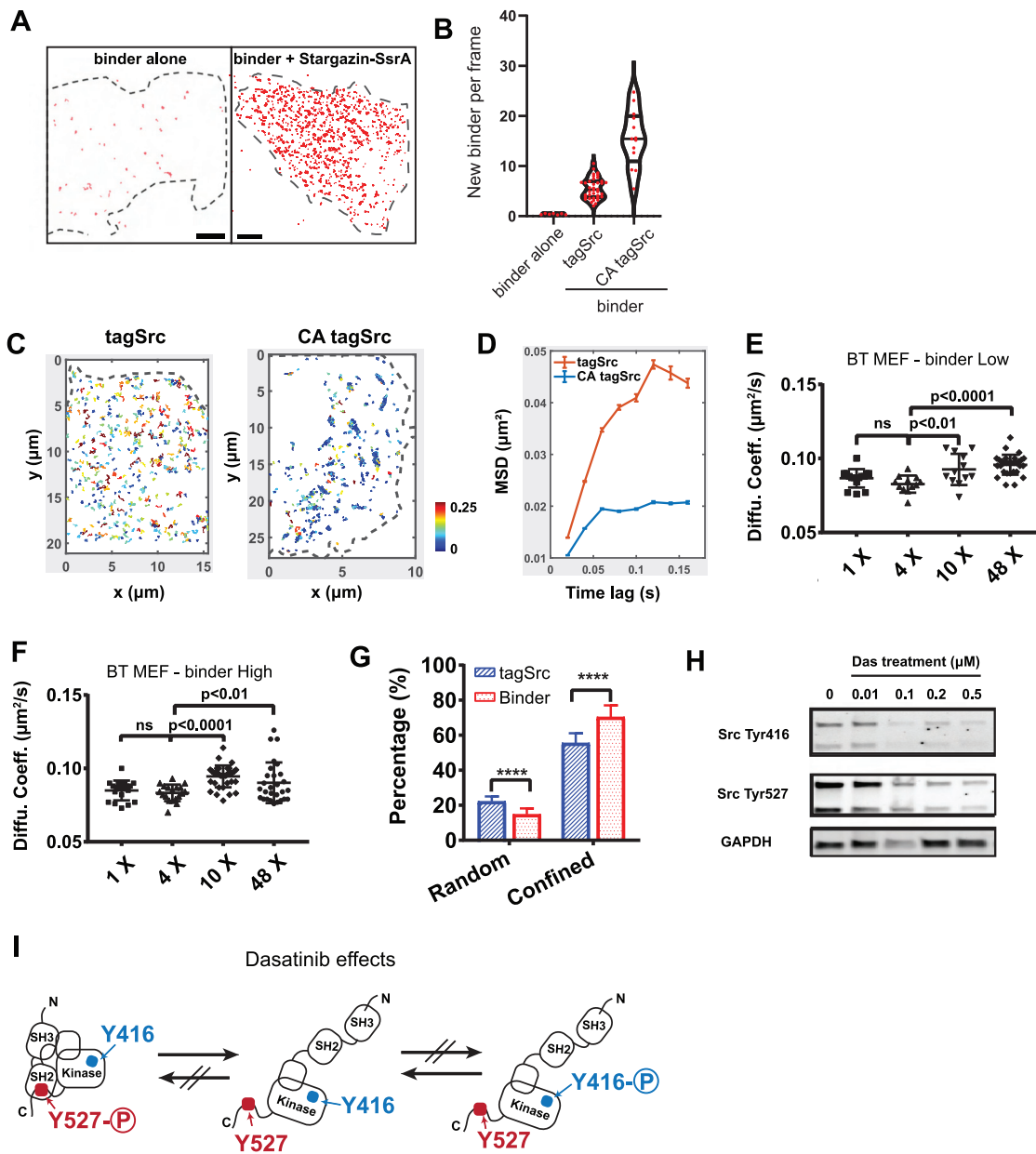


Figure S4. Controls and additional binder/tag SPT results, related to Figure 4

(A) SspB shows little nonspecific binding to the plasma membrane. COS-7 cells were transiently transfected with binder alone (*left*) or co-transfected with SsrA fused to the membrane anchor Stargazin (*right*).

(B) New binder events per frame from cells expressing binder alone, binder and WT tagSrc, binder and CA tagSrc.

(C) Single particle tracking of tagSrc-yPet (*left*) and CA tagSrc-yPet (*right*) in transiently transfected COS-7 cells.

(D) Mean squared displacement analysis of tagSrc-yPet and CA tagSrc-yPet.

(E and F) Diffusion coefficients extracted by MSD analysis for tagSrc-Halo-JF646 and binder-SNAP-JF549 in (E) “binder-Low” and (F) “binder-High” BT MEF cells as a function of doxycycline-dependent expression of both tagSrc and binder. Data shown with Mean \pm SD.

(G) Moment scaling spectrum analysis of tracks shown in Figure 4D, quantifying random and confined diffusive populations. Directionally diffusing molecules were ignored.

(H) Dose-dependent dephosphorylation of Src Tyr-416 and Tyr-527 by dasatinib in BT-MEFs.

(I) Dasatinib generates an open, catalytically inactive Src (middle structure) that binds to downstream targets and to the binder.

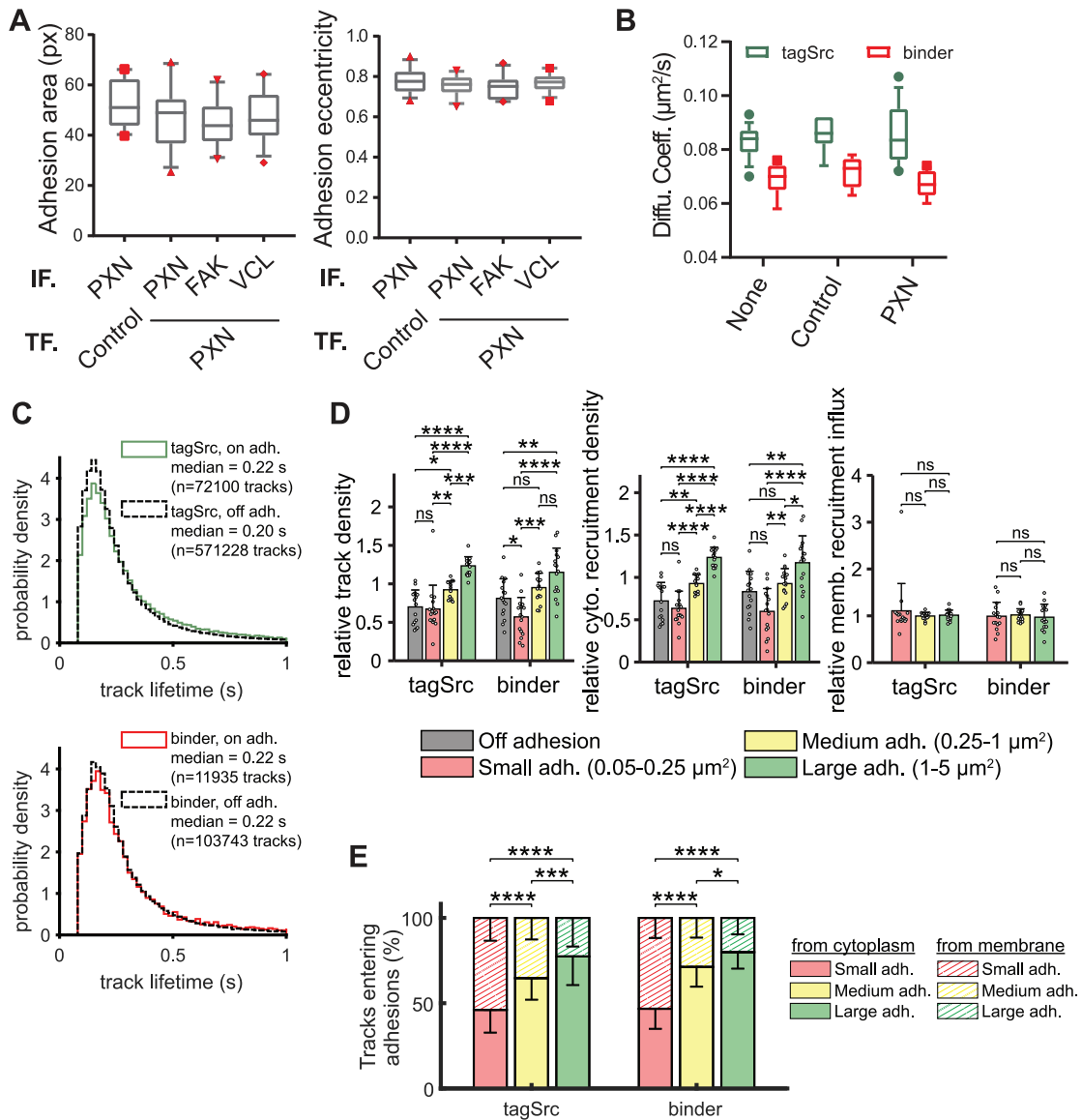


Figure S5. Controls and additional data for correlation of adhesion imaging and binder/tag single particle tracking, related to Figure 5

(A and B) BT MEF cells were transfected with paxillin-EGFP or control vectors (A: blank pBabe vector; B: a vector carrying only the fluorescent protein dTurquoise). Expression of paxillin-EGFP did not perturb (A) the morphology of endogenous adhesions or (B) the diffusion of tagSrc and binder. Adhesion morphologies were characterized by immuno-staining BT MEFs with different adhesion protein antibodies (see STAR Methods). IF, immunofluorescence; TF, transfection; PXN, paxillin; FAK, focal adhesion kinase; VCL, vinculin. Box-and-whisker plots shown with outliers displayed as dots.

(C) Lifetimes of tracks in and out of adhesions. Track density is a reasonable proxy for concentration.

(D) Src activity and recruitment as a function of adhesion size. Track density was computed as the number of track centroids per unit adhesion area (left). Cytoplasmic recruitment density was computed as the number of track starts per unit adhesion area (middle). Membrane recruitment influx was computed as the number of tracks that entered adhesions by lateral diffusion per unit adhesion perimeter (right). For all quantities, “relative” denotes normalization to the average across all adhesions. Both the track density and the cytoplasmic recruitment density increased with adhesion size, for both tagSrc and binder. Adhesions were identified through TIRF imaging of adhesion markers, as described in materials and methods. Bars show mean \pm 1 s.d. Significance judged by one-way ANOVA, * $p < 0.05$, ** $p < 0.01$, *** $p < 0.001$, **** $p < 0.0001$ with Tukey-Kramer correction for multiple hypotheses. Data represent $n = 16$ cells.

(E) Proportions of tracks entering adhesions from the cytoplasm versus membrane as a function of adhesion size. Adhesions were revealed by a single TIRF snapshot. Bars show mean \pm 1 s.d. Significance judged by one-way ANOVA with Tukey-Kramer correction for multiple hypotheses, * $p < 0.05$, ** $p < 0.01$, *** $p < 0.001$, **** $p < 0.0001$.

(F) Track densities and cytoplasmic recruitment densities of tagSrc and binder in cells with adhesions marked by FAK-EGFP ($n = 9$ cells) and Vinculin-EGFP ($n = 10$ cells). Adhesions were revealed by a single TIRF snapshot. Bars show mean \pm 1 s.d. Significance judged by one-way ANOVA with Tukey-Kramer correction for multiple hypotheses, * $p < 0.05$, ** $p < 0.01$, *** $p < 0.001$, **** $p < 0.0001$.

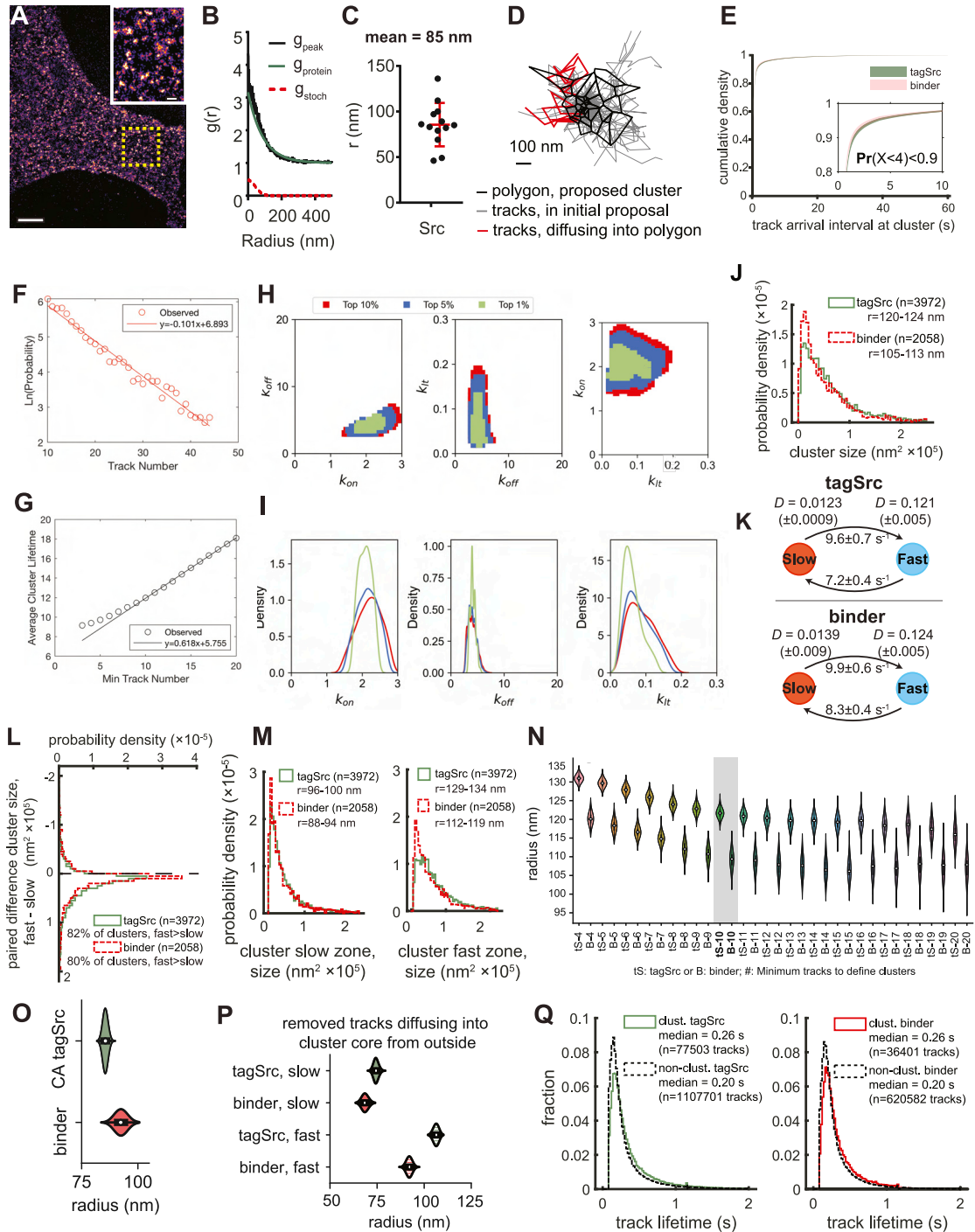


Figure S6. Additional data for the nanoscale organization and activation of Src within clusters, related to Figure 6

(A) Pair-correlation PALM of fixed MEF cells transiently transfected with Src-mGeosM. Scale bar, 5 μm . Inset is a magnified view of the area marked by the dashed yellow box, showing Src clusters. Scale bar, 1 μm .

(B) The autocorrelation function g_{peak} of molecules in the ROI of (A) was measured, enabling calculation of the correlation due to stochastic re-appearances of a single protein g_{stoch} and the actual protein correlation g_{protein} .

(C) The cluster size of Src was estimated from multiple fixed cells, each dot indicating a measurement from a 3 μm x 3 μm area. Results are from 7 cells and 14 areas. Shown is mean \pm 1 s.d.

(D) Example illustrating spatial refinement. During the cluster identification pipeline, densely packed tracks (gray) produced small islands of Voronoi polygons (black). Tracks that diffused into the island (red) could be left out of the cluster proposal because their centroids were further away. These tracks were added into the cluster during spatial refinement, prior to temporal clustering.

(legend continued on next page)

(E) Distribution of track arrival intervals at proposed clusters, prior to temporal clustering. The arrival interval is the time between new observations of tracks. Most arrival intervals (> 90%) are less than 4 s, which was chosen as the cutoff to temporally separate clusters.

(F) The number of tagSrc tracks versus the natural log of the frequency of observation, used for estimating the probability of success P_{suc} (Equation 1).

(G) The minimum number of tracks used to define clusters versus the average observed cluster lifetime, used to estimate the probabilistic cluster lifetime parameters T_M and T_0 .

(H) Regions of parameter space corresponding to the top 10%, 5%, and 1% of simulations matching the data after fitting to the data in Figure 6C, constraining the probability of cluster colocalization to < 1.5%, and requiring the probability of failure P_F to fall between 0.4 and 0.8.

(I) One-dimensional kernel density estimates of the distributions in (H).

(J) Size distributions of tagSrc and binder clusters, from thresholding clusters at half maximal density.

(K) Two-state diffusional analysis of tagSrc and binder using a hidden Markov model, giving diffusion coefficients (D , $\mu\text{m}^2/\text{s}$) and transition rates, mean \pm 1 s.d.

(L) Paired-difference cluster size distributions, showing the difference between fast and slow zones on a per-cluster basis. In most clusters the fast zone is larger than the slow zone.

(M) Size distributions of the slow- and fast-diffusing components of clusters. Sizes were obtained by thresholding clusters at half maximum density.

(N) Cluster sizes of tagSrc and binder across a different minimal track criteria for defining clusters ($n = 4$ to $n = 20$ tracks minimum). Distributions represent bootstrapped medians after thresholding clusters at 50% maximum density.

(O) Cluster sizes for constitutively active tagSrc (CA tagSrc) and binder in the same cells, using the same fluorophores and conditions as in the wild-type tagSrc experiments. Distributions represent bootstrapped medians after thresholding clusters at 50% maximum density.

(P) Slow and fast diffusive zone sizes after removing tracks that diffused into clusters along the plasma membrane. Distributions represent bootstrapped medians after thresholding clusters at 50% maximum density.

(Q) Track lifetimes show clusters stabilize both tagSrc and binder in the plasma membrane.

Data in panels E-R represent $n = 61$ cells.

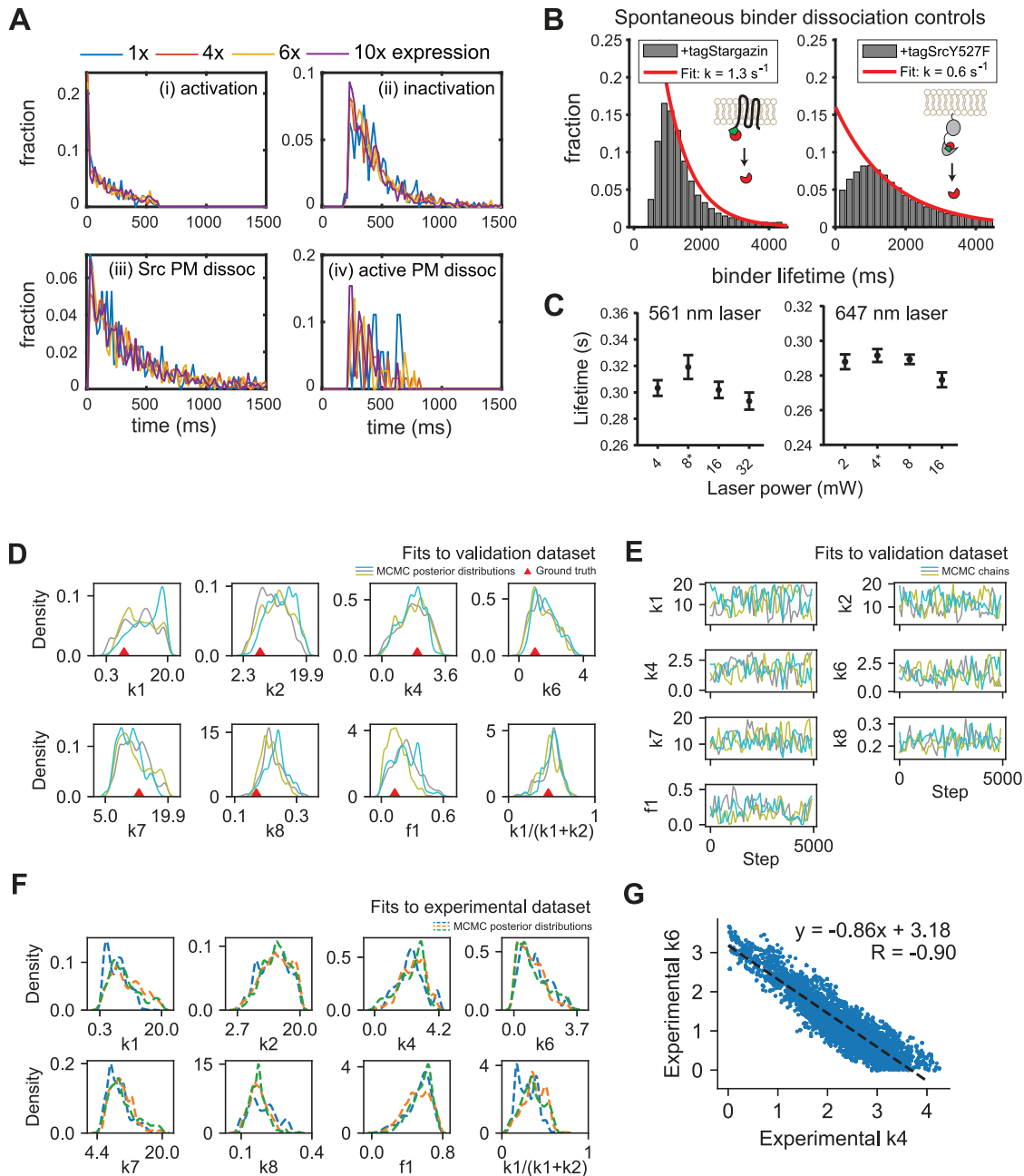


Figure S7. Controls and additional data for kinetic analysis in living cells, related to Figure 7

(A) Titrating doxycycline to adjust tagSrc and binder expression levels does not significantly alter the measured process durations.
 (B) Control experiments measuring spontaneous binder dissociation. Binder track lifetimes when co-expressed with tagStargazin in COS-7 cells (*left*). Binder track lifetimes when co-expressed with tagSrc-Y527F in COS-7 cells (*right*). Binder was labeled with SNAP-JF549.
 (C) The working laser power (6 mW for tagSrc, 2 mW for binder) did not significantly influence lifetime estimates. A 0.02 s change corresponded to a 1-frame change. $N \geq 3$, shown is mean \pm 1 s.d.
 (D and E) Parameter posterior distributions (D) and chains (E) from three independent MCMC fits to the validation data.
 (F) Parameter posterior distributions from three independent MCMC fits to the experimental data. Parameters that were not well constrained (k_1 , k_2 , and k_7) also showed large variability when parameter estimation was performed using simulated data, suggesting that our inability to identify these parameters was due to the structure of the data and not our inference method. Consistent with this, the ratio of k_1 to k_2 was better constrained by the data.
 (G) Linear regression of tagSrc:binder dissociation (k_4) versus one-step Src inactivation + tagSrc:binder dissociation (k_6) parameters from the experimental data MCMC fits (F). R is the Pearson's correlation coefficient.